When is a control not a control? Reactive microglia occur throughout the control contralateral visual pathway in experimental glaucoma

James R Tribble[1, ‡], Eirini Kokkali[2, ‡], Amin Otmani[1], Flavia Plastino[1], Emma Lardner[1], Rupali Vohra[3,4], Miriam Kolko[4,5], Helder André[1], James E Morgan[2,6], Pete A Williams[1,*]

[1] Department of Clinical Neuroscience, Division of Eye and Vision, St. Erik Eye Hospital, Karolinska Institutet, Stockholm, Sweden

[2] School of Optometry and Vision Sciences, Cardiff University, Cardiff, Wales, U.K.

[3] Department of Veterinary and Animal Sciences, Pathobiological Sciences, University of Copenhagen, Denmark

[4] Department of Drug Design and Pharmacology, University of Copenhagen, Copenhagen, Denmark

[5] Department of Ophthalmology, Rigshospitalet-Glostrup, Copenhagen, Denmark

[6] School of Medicine, Cardiff University, Cardiff, Wales, U.K.

[‡] Authors contributed equally to this work

[*] *Correspondence to:*
Pete A Williams, Department of Clinical Neuroscience, Division of Eye and Vision, St. Erik Eye Hospital, Karolinska Institutet, Stockholm, Sweden; pete.williams@ki.se; @pete_the_teapot

Emails
james.tribble@ki.se (JRT), kokkalie@cardiff.ac.uk (EK), amin.otmani@ki.se (AO), flavia.plastino@ki.se (FP), emma.lardner@sll.se (EL), rvohra@sund.ku.dk (RV), miriamk@sund.ku.dk (MK), helder.andre@ki.se (HA), morganje3@cardiff.ac.uk (JEM), pete.williams@ki.se (PAW)

Funding
Vetenskapsrådet 2018-02124 (PAW). Fight For Sight UK 512264 (JEM). Fight For Sight Denmark (MK). Pete Williams is supported by the Karolinska Institutet in the form of a Board of Research Faculty Funded Career Position and by St. Erik Eye Hospital philanthropic donations. Rupali Vohra is a part of the BRIDGE – Translational Excellence Programme at the Faculty of Health and Medical Sciences, University of Copenhagen (Novo Nordisk Foundation NNF18SA0034956).

Abstract

Background: Glaucoma remains a leading cause of irreversible blindness worldwide. Multiple animal models show retinal ganglion cell injuries that replicate features of glaucoma. In these experiments the contralateral eye is commonly used as an internal control. As in humans; in rodents and non-human primates there is significant cross-over of retinal ganglion cell axons from the ipsilateral to the contralateral side at the level of the optic chiasm which may confound findings when damage is restricted to one eye. While neuroinflammation may be a critical event that damages retinal ganglion cells and their axons during glaucoma progression the effect of unilateral damage on the contralateral visual pathway has largely been unexplored.

Methods: Ocular hypertensive glaucoma was induced unilaterally or bilaterally by intracameral injection of paramagnetic beads in adult Brown Norway rats. Retinal ganglion cell neurodegeneration and dysfunction were assessed. Neuroinflammation was quantified in the retina, optic nerve head, optic nerve, lateral geniculate nucleus, and superior colliculus by high resolution imaging, and in the retina by flow cytometry and protein arrays.

Results: Following ocular hypertensive stress the retinal vasculature remodels, peripheral monocytes enter the retina, and microglia become highly reactive. This effect is more marked in animals with bilateral induction of ocular hypertensive glaucoma. In rats where glaucoma was induced unilaterally there was significant microglia activation in the contralateral (control) eye. Microglial activation extended into the optic nerve and terminal visual thalami, where it was similar across hemispheres irrespective of whether ocular hypertension was unilateral or bilateral.

Conclusions: Ocular hypertensive glaucoma in the rat recapitulates many of the features of human glaucoma. In this model microglia become reactive throughout the visual pathway during glaucoma pathogenesis. These effects are not isolated to the experimental eye and its pathway and significant neuroinflammation occurs in the contralateral 'control' eye and pathway. These data suggest that caution is warranted when using the contralateral eye as control in unilateral models of glaucomatous damage.

Key words: microglia, monocyte, neuroinflammation, glaucoma, retina, optic nerve, optic nerve head, lateral geniculate nucleus, superior colliculus, dendrite, synapse

Background

Glaucoma is the leading cause of irreversible blindness, affecting ~80 million people worldwide (1). The underlying pathology is complex and characterised by the progressive dysfunction and loss of retinal ganglion cells and their axons. Major risk factors are increasing age, elevated intraocular pressure, and genetic predisposition. Despite strategies to lower intraocular pressure (the only treatable risk factor for glaucoma), over 40% of treated glaucoma patients will go blind in at least one eye (2) suggesting that factors other than high intraocular pressure drive retinal ganglion cell degeneration.

Neuroinflammation is a shared feature of glaucoma pathogenesis in human glaucoma patients (3) and animal models of glaucoma (genetic and inducible (4)). In times of stress, retinal ganglion cells are reliant on a supportive network of glial cells to provide neurotrophic and metabolic support, especially to their long, unmyelinated axons in the retina and optic nerve head. Emerging evidence supports a paradigm in which retinal ganglion cell axons are insulted throughout their trajectory to retinorecipient areas; the dorsal lateral geniculate nucleus and the superior colliculus. Microglia and/or other immune-derived cells are likely to be key players in these pathogenic events.

The eye is commonly used as a tool to explore neurodegenerative events. However, a common feature of these experiments is the use of the contralateral eye as an internal control (which is often used to normalise data to the experimental eye). These data should be qualified because: (i) retinal ganglion cell numbers differ between eyes even within individual animals (5), (ii) significant numbers of retinal ganglion cell axons do not cross at the optic chiasm and terminate in ipsilateral thalami (ranging from ~3% in mouse and ~3-10% in rat to ~45% in primates and ~50% in human (6-8)), (iii) albino rodents are commonly used (*e.g.* Wistar and Sprague-Dawley rats) which have reduced ipsilateral projections (9-12), and, (iv) most human primary open angle glaucoma is bilateral. Microglial activation is an early and persistent feature across glaucoma models and species with evidence of immune-cell activation in human tissue from advanced glaucoma (13-17). To date, there is a paucity of data regarding microglial activation in the contralateral eye of mice with unilateral ocular hypertension (largely qualitative with quantification only through cell counting (18-20)). Activation has been reported in the optic nerve and in terminal brain thalami (15, 21, 22), but contralateral activation has yet to be fully explored in these tissues.

To address these issues and explore any neuroinflammation throughout the visual pathway in glaucoma, we fully characterise inflammatory changes in an inducible rat model of ocular hypertensive glaucoma in which intraocular pressure is elevated by intracameral (anterior chamber) injection of paramagnetic beads to occlude the drainage structures of the eye (23, 24). This results in sustained ocular hypertension driving a reproducible and significant loss of retinal ganglion cell numbers as well as neuroinflammation (without uveitis). Using this model, we

assessed the effects of unilateral or bilateral induced ocular hypertension on glaucoma pathology throughout the retinal ganglion cell projections. These experiments were performed in the Brown Norway rat as it is the genetic standard for rats, is inbred, pigmented, and avoids retinothalamic pathway issues present in albino animals. We demonstrate that neuroinflammation persists throughout retinal ganglion cell pathways with monocyte infiltration and pro-inflammatory cytokine release in the retina. Critically, these changes are mirrored in the contralateral visual pathway warranting caution when using the contralateral eye as a 'control' in ophthalmic research.

Methods

Rat strain and husbandry

Adult, male Brown Norway rats (aged 12-16 weeks, weighing 300-375 g, SCANBUR) were housed and fed in a 12 h light / 12 h dark cycle with food and water available *ad libitum*. All experimental procedures were undertaken in accordance with the Association for Research for Vision and Ophthalmology Statement for the Use of Animals in Ophthalmic and Research. Individual study protocols were approved by Stockholm's Committee for Ethical Animal Research (10389-2018).

Induction of ocular hypertension

Ocular hypertension (OHT) was induced bilaterally (OHT/OHT; *n* = 22 rats, 44 eyes) or unilaterally (OHT/NT; *n* = 12 rats, 12 eyes). For unilateral OHT rats, the contralateral eye was an un-operated, normotensive (NT) eye (NT/OHT; *n* = 12 rats, 12 eyes). Bilateral NT rats served as controls (NT/NT; *n* = 17 rats, 34 eyes). OHT was induced using a magnetic microbead injection model (23, 24) with modifications detailed below. Microbeads (4.5 µm diameter) (Dynabead Epoxy M-450, Thermo Fisher) were prepared for injection by washing with 1x Hank's balanced salt solution (HBSS -$CaCl_2$ -$MgCl_2$ -phenol red, Gibco) and re-suspended in 0.25x volume of HBSS (~2.7 x 10^6 beads/µl). These beads were selected as the coating of glycidyl ether groups confers a hydrophobic nature that allow for easy dispersion within the anterior chamber while retaining blockage of the iridocorneal angle through binding amine and sulphydryl groups on cell surfaces. Rats were anaesthetised with an intraperitoneal injection of ketamine (37.5 mg/kg) and medetomidine hydrochloride (1.25 mg/kg). Using a nanofil syringe (NanoFil; WPI) with 33 G tribevelled needle (WPI), 6-8 µl of bead solution was injected into the anterior chamber of the eye using a tunnel incision through the cornea. Beads were distributed to block the iridocorneal angle using a handheld rare earth magnet (cylindrical with a 4 mm diameter). Intraocular pressure (IOP) was measured using a Tonolab rebound tonometer (Icare) in awake and unrestrained rats. Rats were habituated to the tonometry procedure the week before surgery. Baseline IOP was recorded on the day of surgery (day 0) and recorded every 2-4 days afterwards until the endpoint (postoperative day 14), with IOP recordings always taken between 9 and 10am to avoid the effects of the circadian rhythm on IOP (2-3 hours from lights on). IOP was taken as the average of 5 tonometer readings. NT/NT rats followed the same 14 day time course (without surgery). In a subset of animals (*n* = 6 NT/NT and 6 OHT/OHT eyes) IOP was recorded 6, 24, and 72 hours post-induction.

General histopathology

Rats were heavily anaesthetized at day 14 by intraperitoneal injection of pentobarbital (75 mg/kg), and euthanised by cervical dislocation. Eyes were immediately enucleated (with 1 mm of optic nerve post-globe preserved) and immersed in 3.7% PFA in 1x PBS. Brains (with attached optic nerves) were removed and immersed in 3.7% PFA in 1x PBS. Eyes, optic nerves, and brains for

cryo-sectioning were maintained in fixative for 24 hours before cryo-protecting in 30% sucrose in 1x PBS for 24 hours, freezing in optimal cutting temperature medium (Sakura) on dry ice, and stored at -80 ˚C. Cryo-sections were cut on a cryostat (Cryostar NX70, Thermo Scientific) and stored at -20 ˚C. Eyes were sectioned at 20 µm thickness (anterior to dorsal plane), with sections maintained from ~200 µm nasal to ~200 µm temporal of the optic nerve head (*n* = 3 eyes for NT/NT, OHT/OHT, NT/OHT, and OHT/NT). Optic nerves for cryo-sectioning were maintained as pairs attached at the optic chiasm, and sectioned at 20 µm to generate longitudinal nerve sections (*n* = 4 optic nerves for NT/NT, OHT/OHT, NT/OHT, and OHT/NT). Brains were serial sectioned (coronal plane) at 50 µm from -4 mm caudal of cranial landmark Bregma, to -8 mm caudal of Bregma in order to capture the entire dLGN and SC (*n* = 3 brains [6 independent hemispheres] for NT/NT, OHT/OHT, NT/OHT, and OHT/NT). Eyes for paraffin sectioning (*n* = 6 NT/NT eyes, 10 OHT/OHT eyes) were prepared in paraffin and sectioned (anterior to dorsal plane) to give optic nerve head sections (3 µm thickness) on a microtome (Microm HM 355S, Thermo Scientific). Optic nerves for paraffin sectioning (*n* = 4 NT/NT nerves, 5 OHT/OHT nerves) were dissected free from the brain 2 mm post-optic chiasm. Optic nerves were separated at the chiasm with a diagonal cut used to maintain orientation and prepared in paraffin for sectioning. Transverse sections were cut (3 µm thickness) from the end proximal to the eye.

Immunohistochemistry and immunofluorescence

Antibodies and stains used for immunofluorescence, immunohistochemistry, and histological labelling are detailed in **Table 1**. The same immunofluorescent labelling protocol was followed for cryo-sections, paraffin sections, and flat mount retina with exceptions noted where relevant. Tissue was isolated using a hydrophobic barrier pen (VWR), permeabilised in 0.5% Triton X-100 in 1x PBS for 1 h, blocked in 5% bovine serum albumin in 1x PBS for 1 h, and primary antibody applied overnight at 4 ˚C (see **Table 1**). Tissue was then washed for 5 x 5 min in 1x PBS, secondary antibody applied (1:500 in 1x PBS) for 4 h at room temperature, and washed for 5 x 5 min in 1x PBS. DAPI nuclear stain (500 µg/ml stock; used 1:500 in 1x PBS) was applied for 10 min, the tissue washed for 5 min in 1x PBS, dried and mounted using Fluoromount-G and glass coverslips (Invitrogen). For cryo-sections, tissue was air dried for 15 min and rehydrated in 1x PBS for 15 min before following the protocol above. For paraffin sections, sections were deparaffinised, rehydrated through xylene and an alcohol gradient before performing antigen retrieval using EDTA buffer (pH 9, 20 min, 100 °C). Immunohistochemistry was performed in a Bond III robotic system (Leica Biosystems, Newcastle, UK).

Table 1. Antibody details

Antibody	Target	Host	Dilution	Details	Use
βIII-tubulin	Microtubules specific to RGCs	Chicken	1:250	Novussbio cat # NB100-1612	IF
PE CD11b/c	CD11b (clone OX-42)	Mouse	1:400	Nordic BioSite cat # 201807	FC
AF 647 CD45	CD45 (clone OX-1)	Mouse	1:2000	Nordic BioSite cat # 202211	FC
BV 421 CD90.1	Thy1.1 (clone OX-7)	Mouse	1:200	Nordic BioSite cat # 202529	FC
GS	Glutamine synthethase	Rabbit	1:5000	Sigma-Aldrich cat # G2781	IF
GFAP	Glial fibrillary acidic protein	Rabbit	1:1000	Abcam cat # ab 207165	IF
Isolectin GS-IB_4 (IsoB4)	Poly-*N*-acetyllactosamine, found on microglia, endothelial cells, monocytes/macrophages	Lectin from *Griffonia simplicifolia* conjugated to biotin	0.1mg/ml	Invitrogen cat # I21414	IF
NeuroTrace™ 530/615 red fluorescent Nissl stain	Nissl material	NA	1:100	Molecular Probes cat # N-21482	IF
NF-M	Neurofilament medium chain	Chicken	1:500	Novusbio cat # NB300-222	IF
MBP	Myelin basic protein	Rabbit	1:4000	Abcam cat # ab210811	IF
MAP2	Neuronal dendrites	Chicken	1:250	Novusbio cat # NB300-213	IF
RBPMS	RNA-binding protein, RGC specific in the retina	Rabbit	1:500	Novusbio cat # NBP2-20112	IF, IHC

Synaptophysin 1	Synaptophysin 1, pre-synaptic protein	Rabbit	1:500	Synaptic Systems cat # 101 002	IF
Goat-anti Rabbit AF 488	Rabbit primary antibody	Goat	1:500	Abcam cat # A11008	IF
Goat-anti Rabbit AF 568	Rabbit primary antibody	Goat	1:500	Abcam cat # A11011	IF
Goat-anti Chick AF 488	Chick primary antibody	Goat	1:500	Abcam cat # A11039	IF
Goat-anti Chick AF 568	Chick primary antibody	Goat	1:500	Abcam cat # A11041	IF
Streptavidin AF 488 conjugate	Biotin	NA	4 µg/ml	Invitrogen cat # S11223	IF

FC (flow cytometry), IHC (immunohistochemistry), IF (immunofluorescence)

Assessment of neurodegeneration following ocular hypertension.

Eyes for flat mount retina preparations (*n* = 6 NT/NT eyes, 6 OHT/OHT eyes, 5 NT/OHT eyes, 5 OHT/NT eyes all at 14 day time point, and 8 OHT/OHT eyes at 3 day time point) were maintained in fixative as globes for 2 h before the retina was dissected free at the optic nerve head, the vitreous removed, and the retina flat mounted ganglion cell layer up on a coated glass slide (Superfrost+, Thermo Fisher). Retinas were labelled with antibodies against RBPMS and Isolectin B4, and counterstained with DAPI. Flat mounted retinas were imaged on a Zeiss Axioskop 2 plus epifluorescence microscope for quantification of retinal ganglion cell densities. Six images per retina (40X magnification, 0.25 µm/pixel) were taken equidistant to the optic nerve head (1000 µm eccentricity). Images were cropped to 150 μm^2 and RBPMS+ cells and DAPI nuclei counted using the cell counter plugin for Fiji (25). Cell counts were averaged across the 6 images, and expressed as a density per 100 μm^2. On cryo-sections (*n* = 4 NT/NT eyes, 4 OHT/OHT eyes), neurofilament labelling at the optic nerve head was imaged by epifluorescence microscopy (as above). On paraffin sections (*n* = 6 NT/NT eyes, 10 OHT/OHT eyes), H&E and Nissl staining were performed and imaged on an Olympus IX73 (20X, tiled colour image, 0.51 µm/pixel). The optic nerve head qualitatively assessed as either normal or cupped. Optic nerve axon loss was assessed in 3 µm transverse paraffin sections (*n* = 4 NT/NT nerves, 5 OHT/OHT nerves). Sections were labelled with antibodies targeting NF-M and MBP and airyscan images acquired on a Zeiss LSM800-Airy (63X, 1.3X optical zoom, 35 nm / pixel). Five 66.76 μm^2 images were collected per nerve. Axons were counted using ImageJ's cell counter plugin (in Fiji) and averaged. Dendrite and synapse loss were quantified by MAP2 and Synaptophysin1 staining in the inner plexiform layer (*n* = 3 NT/NT eyes, 3 OHT/OHT eyes) and images were acquired on a Zeiss LSM800-Airy (20X, 319.45 μm^2, 0.312 µm/pixel, *z*-stack). Image parameters were kept constant. Images were *z*-compressed (sum slices) and the inner plexiform layer cropped. Images were thresholded to a

constant range, binarised, and a watershed separation performed before analysing particles using the ImageJ particle analyser (in Fiji). The number of particles/100 μm^2, average size of particles (μm^2), and fractal analysis (fractal box count) were performed to determine dendrite and synapse integrity and space filling.

Vasculature analysis

For retinal blood vessel analysis (*n* = 10 NT/NT eyes, 8 OHT/OHT eyes), images were captured on a Zeiss Axioskop 2 plus epifluorescence microscope (5X magnification, 2861.86 x 2144.33 µm area, 2.05 µm/pixel). Images were stitched in Fiji using the pairwise stitching plugin (26). The Isolectin B4 / blood vessel channel was isolated from the image in Fiji and background from the image removed by thresholding. Retinas were cropped to 3000 μm^2 to maintain consistency (representing >80% of retinal explant area). AngioTool (27) was used to measure blood vessel morphologies (total blood vessel length, junction density, lacunarity (a measure of space filling within the image, where a high lacunarity equals less space filling by blood vessels)) with the following parameters: blood vessel diameter (8-30 µm) and pixel intensity (0-255).

Retinal stretch

Ocular globe measurements were recorded using digital callipers (VWR; resolution 0.01mm). Eye diameter at the limbus was measured before anterior chamber bead injections in anaesthetised animals (*n* = 20 OHT eyes, and following enucleation after euthanasia (*n* = 31 NT eyes, 35 OHT eyes). Axial length (diameter from cornea to optic nerve) was also measured post-enucleation (*n* = 31 NT eyes, 35 OHT eyes). To determine whether retinal stretch also occurred in OHT, eyes were processed for paraffin sectioning as above (*n* = 6 NT eyes, 8 OHT eyes). Sections through the optic nerve head (3 µm thickness; *n* = 6 NT/NT eyes, 10 OHT/OHT eyes) were labelled for RBPMS, counter stained with X, and imaged on an Olympus IX73 (20X, tiled colour image, 0.51 µm/pixel). Retinal length was measured in Fiji and RBPMS counts across the whole retina performed using the cell counter plugin and expressed as a density. *Spearman's* correlations were performed in R for comparisons of eye size, IOP measures, RBPMS density, retinal length and animal weight. Multiple regression analysis was performed in R using the *lm* function and relative importance calculated using the *calc.relimp* function in the relaimpo package (28).

Cholera toxin tracing

Intravitreal injection of cholera toxin was used as a neuronal tracer to visualise retinal ganglion cell projections and measure axon transport. At day 11, rats were anaesthetised as above and 3 µl of Alexa Fluor 488 or 594 conjugated cholera toxin, subunit β, (CT-β; Invitrogen) was injected intravitreally using a NanoFil syringe with 33 G tribevelled needle. CT-β was injected rapidly and the syringe withdrawn after 30 seconds. CT-β AF488 was injected into the left eye and CT-β AF594 into the right eye (*n* = 6 eyes for NT/NT and OHT/OHT). Rats were euthanised on day 14 as above. Flat mounted optic nerves and optic chiasms, and flat mounted SC were imaged on Zeiss Axioskop 2 plus epifluorescence microscope (5X and 2.5X magnification respectively). Eyes,

optic nerves, and brains (n = 6 per group) were cryo-sectioned (20 µm thickness) and stored as above. CT-β labelling at the optic nerve head was imaged on a Zeiss LSM800-Airy (10X, 0.62 µm/pixel) and qualitatively assessed to have either normal or incomplete axon transport. Transverse optic nerve sections, brain sections, flat mounted optic nerves and optic chiasms, and flat mounted SC were imaged on Zeiss Axioskop 2 plus epifluorescence microscope (optic nerves, 10X, 1.03 µm/pixel; dLGN, 5X, 2.05 µm/pixel; SC, 2.5X, 4.25 µm/pixel;) and qualitatively assessed to have/not have axonal transport to the brain (for both dLGN and SC).

Microglia imaging and quantification

All microglia images were acquired on a Zeiss LSM800-Airy (20X, 319.45 μm^2, 0.312 µm/pixel, *z*-stack). Imaging parameters were kept constant to allow comparison of microglial volume. For flat mounted retinas labelled with Isolectin B4, RBPMS, and DAPI, 4 images were taken at 1500 µm superior, nasal, inferior, and temporal to the optic nerve head. In longitudinal optic nerve sections, Isolectin B4 was imaged proximal to the eye and proximal to the chiasm. Images of Isolectin B4, Nissl, and DAPI labelled brain sections were acquired at the midpoint of the SC and dLGN respectively. Microglia from retina and brain regions were reconstructed manually in Imaris (Bitplane) using the Filaments tool with automatic volume filling and *z*-depth. Parameters were kept constant for direct comparison of volumes. Microscopy, reconstructions, and image analysis were performed independently by 3 independent researchers and final reconstructions curated by an independent researcher. In the retina, microglia were classified to either the nerve fibre layer/ganglion cell layer (NFL/GCL) or inner plexiform layer based on *z*-depth, using the lower boundary of RBPMS nuclei as the limit of the ganglion cell layer. In the retina, ~9 microglia per image were reconstructed in the NFL/GCL on average (n = 137 NT/NT, 185 NT/OHT, 197 OHT/NT, 222 OHT/OHT) and ~7 microglia per image in the inner plexiform layer on average (n = 92 NT/NT, 134 NT/OHT, 160 OHT/NT, 170 OHT/OHT). In the brain, ~5 (SC) and ~6 (dLGN) microglia were reconstructed per image on average (SC, n = 103 NT/NT, 114 NT/OHT, 115 OHT/NT, 121 OHT/OHT; dLGN, n = 123 NT/NT, 116 NT/OHT, 138 OHT/NT, 130 OHT/OHT). For individual microglia, total number of branch points, total process length, total process volume, and field area were exported. Total process volume was normalised to total process length in order to distinguish microglia with large but thin processes from those with short but thick processes. Sholl analysis was performed with the soma centre as the origin point and an intersection distance of 3 µm. The area under the Sholl curve (Sholl AUC) was calculated. Individual microglia were grouped by unsupervised hierarchical clustering (HC) in order to define populations of increasing reactivity. HC was performed using Morpheus (https://software.broadinstitute.org/morpheus) where every microglia from the GCL was classified based on the 5 morphological measurements described above. For HC, microglia were clustered using Euclidean distance (linkage method = average). In longitudinal optic nerve sections an area of 312(x) x 624(y) x 12.25(z) μm^3 was cropped (to avoid including the optic nerve sheath). The whole channel corresponding to Isolectin B4 was reconstructed as a volume using the Surfaces automatic volume analysis tool in Imaris. Image thresholding was kept constant. Because adjacent cells were sometimes considered as one

object by the Surfaces algorithm, the number of microglia within the same area was counted manually using the Imaris Spots tool.

Quantification of infiltrating and reactive immune cells

Microglia and monocyte density was calculated by counting all microglia and monocytes in the image volume, taking the average of the 4 regions imaged, and expressing as $n/100\ \mu m^3$ (n = 6 NT/NT eyes, 6 OHT/OHT eyes, 5 NT/OHT eyes, 5 OHT/NT eyes; n = 3 brains [6 independent hemispheres] for NT/NT, OHT/OHT, NT/OHT, and OHT/NT)). Microglia in the retina were classified to the NFL/GCL or inner plexiform layer as above. Microglia and monocyte soma centre positions were recorded and related to RBPMS+ nuclei centres in the retina. For each microglia, nearest neighbour distances (NND) to the nearest microglia and neuron (RBPMS+ in the retina) were calculated in R using the *nndist* function in the spatstat package (29). Monocyte NND was calculated in the same way. Gliosis was determined by glutamine synthetase (GS) staining in the retina (cryo-sections; n = 3 eyes for NT/NT and OHT/OHT) and GFAP staining in optic nerve (transverse paraffin sections; n = 4 NT/NT nerves, 5 OHT/OHT nerves). GS and GFAP labelling were quantified by average pixel intensity and space filling assessed by fractal measurement (Fractal box count). GFAP fibre alignment was measured using OrientationJ (30).

Flow cytometry analysis of microglia and monocyte populations

To assess retinal microglia and monocytes numbers, at day 3 rats were euthanized as above (n = 7 NT/NT eyes, 8 OHT/OHT eyes), whole retinas dissected free from eyes cups under ice-cold HBSS, and dissociated in dispase in 1x HBSS (Corning) at 37 ˚C and 350 RPM on an Eppendorf ThermoMixer C (Eppendorf). Cell were blocked with 1% BSA in 1x HBSS for 1 h and stained with antibodies against CD11b/c, CD45, and CD90.1. Cell numbers were assessed on a BD Influx equipped with 488, 561, 641 and 405 nm lasers. Gates were set based on FS *vs* SS and viability dye exclusion (LIVE/DEAD Aqua, Invitrogen). Microglia were identified as $CD11b/c^{+}/CD45^{lo}/CD90.1^{-}$ cells and monocytes identified as $CD11b/c^{hi}/CD45^{hi}/CD90.1^{-}$ cells. Singlets were discriminated based on FS area *vs* pulse width. Cell samples were run for 600 s while mixing (accounting for approx. 25% of total tissue homogenate) and data analysed using FlowJo (FlowJo LLC).

Cytokine Assay

Cytokine array analysis was performed in order to identify retinal or circulating factors that might influence immune activation in OHT and NT/OHT eyes. Rats were euthanized at day 14 and eyes enucleated (n = 4 eyes for NT/NT, OHT/OHT, NT/OHT, and OHT/NT). Whole retina (without optic nerve head) were dissected in HBSS and lysed in HBSS with protease inhibitors by ultrasonication (Vibra-Cell; Sonics & Materials). Samples were frozen at -80 ˚C overnight, thawed, centrifuged, and protein quantification performed by Bradford assay. The array (Proteome profiler rat XL cytokine array kit; R&D systems) was performed according to manufacturer's instructions. 100 µg of protein was used for each sample and final membranes exposed to *x*-ray

film for 2 s, 5 s, 10 s, 30 s, 1 min, 2 min, 5 min, 10 min, 20 min, and overnight (over-exposure). Developed films were digitised and analysed by densitometry after background subtraction (Fiji). Spots were analysed in duplicates and normalised to the average of the 3 reference spot duplicates. The best exposure was determined by the strength of signal and lack of spot blurring.

Statistical analysis

All statistical analysis was performed in R. Data were tested for normality with a *Shapiro Wilk* test. Normally distributed data were analysed by *Student's t*-test or *ANOVA* (with *Tukey's HSD*). Non-normally distributed data were assessed using a *Kruskal Wallis* test followed by multiple pairwise *Wilcoxon* tests with *Benjamini and Hochberg* correction. Unless otherwise stated, * = $P < 0.05$, ** = $P < 0.01$, *** $P < 0.001$, NS = non-significant ($P > 0.05$).

Results

Unilateral glaucoma does not cause increased intraocular pressure or retinal ganglion cell death in the contralateral eye

Following intracameral injection (**Figure 1A**) paramagnetic beads were directed to the iridocorneal angle (**Figure 1B**). Clinically-relevant histopathology confirmed that beads were maintained in the angle for the duration of the experiment with beads evident within the drainage structures of the trabecular meshwork and Schlemm's canal (**Figure 1B**). This resulted in a significant and robust IOP increase that was sustained until euthanasia (**Figure 1C**). Peak IOP occurred at 3 days post-induction, with no RGC death detected at this 3 day time point, supporting a pathology absent of early ischemia-related RGC death (**Supplementary Figure 1**). There was no significant difference between unilateral and bilateral normotensive eyes (NT), or between unilateral and bilateral ocular hypertensive eyes (OHT) in terms of magnitude or duration of IOP increases. Fourteen days of sustained OHT resulted in excavation of the optic nerve head and thinning of the nerve fibre layer (**Figure 1D-F**). RBPMS labelling demonstrated significant loss of RGCs at 14 days post-injection with RGC density being reduced in both OHT/NT and OHT/OHT eyes compared to NT/NT and NT/OHT eyes, with no significant unilateral or bilateral effect in RGC death (**Figure 1G**). There was a small increase in the nearest neighbour distance (NND) between RGCs in OHT eyes and although this increase was small (30% increase in OHT/OHT compared to NT/NT), the range of values for OHT was increased (doubling of the interquartile range in OHT/OHT). There was no detectable difference in RGC density between superior and inferior retina in OHT eyes. Collectively, these data suggest diffuse and random RGC death (*i.e*. not regional cell loss) (**Figure 1G**).

We have previously demonstrated RGC dendritic atrophy at the single RGC-level (31, 32). Corroborating this, RGC dendritic loss in the inner plexiform layer (IPL) in OHT eyes was observed by a reduction in MAP2 labelling (**Figure 1H**). There was no statistically significant change in synapse number (as assessed by synaptophysin labelling in the IPL) in OHT eyes (**Figure 1H**), with labelling highly variable across groups and measures, suggesting no gross loss of synaptic structure (pre-synaptic to RGCs).

Ourselves and others have previously identified vascular dysfunction in the retina and ONH as a feature of human and animal models glaucoma (33-36). Analysis of Isolectin B4 labelled vessels demonstrated a significant reduction in total vessel length, junction density, and an increase in lacunarity indicting reduced vessel coverage of the inner retina (**Figure 2**).

Retinal ganglion cell degenerative processes extend into terminal brain regions

Retinal ganglion cell neurodegeneration during glaucoma is a compartmentalised event, with OHT driving dendritic and synaptic retraction, soma degeneration, and deafferentation (37). We confirmed loss of RGC axons in the optic nerve by counting individual nerve fibres assessed in

neurofilament labelled sections imaged at ultra-high resolution (35 nm / pixel). The total number of axons was significantly reduced in OHT eyes compared to NT, with no significant change in optic nerve area when measured from the dura mater or pia mater (**Figure 3A**). GFAP labelling in optic nerves demonstrated astrocyte remodelling, with a significant reduction in fibre coherency following periods of OHT, supporting evidence from human glaucoma and those generated from animal models of glaucoma (38, 39) (**Figure 3B**). These data support a model in which there is no uncoupling of axon and soma neurodegenerative events.

We next assessed axonal transport in remaining axons across the whole RGC, including projections to the dLGN and SC (**Figure 3C**). In NT animals, robust labelling was evident throughout the optic nerve (with crossover at the chiasm) and persisted to the SC and dLGN (**Figure 3D**). Labelling was visibly reduced in OHT eyes in the optic nerve, further reducing pre-chiasm with reduced penetrance to the SC indicating markedly reduced axonal transport and axon degeneration (**Figure 3D**). Although sectoral regions of functional axonal transport remained, this was not uniform across optic nerves or brain regions and was further evidenced in cryo-sections of eyes, optic nerves, and brain regions (**Figure 3E**). In OHT eyes, axonal transport was largely intact within the retina, stalling at the optic nerve head myelin transition zone. Optic nerve proximal to the optic nerve head demonstrated this lack of functional transport and sectoral dysfunction that was further reduced distally (indicating both a loss of axons (axon degeneration) and a decrease in axon transport in remaining axons). Labelling in the dLGN was significantly reduced in OHT animals with evidence of some persisting ipsilateral projections. Labelling in the SC was also significantly reduced (**Figure 3E**).

Ocular stretch may confound measurement of retinal ganglion cell densities in ocular hypertensive eyes

Following 14 days of OHT, we grossly observed an increase in the size of OHT eyes and hypothesised that chronic high IOP may lead to scleral remodelling and enlargement of the eye. We therefore recorded calliper measurements of the eyes pre-surgery (dimeter at the limbus) and post-euthanasia at day 14 post-OHT induction (diameter at the limbus and axial length from cornea to optic nerve) and compared to NT controls. OHT eyes demonstrated a significant increase in diameter by 14 days compared to both pre-surgery size (30% increase, $P < 0.001$) and NT controls (19% increase, $P < 0.001$; **Figure 4A**). The difference in the magnitude of increase is likely due to the difference in measurement pre-surgery and post-euthanasia. This is reflected in the significant difference between pre-surgery OHT eyes and NT eyes (9% increase, $P < 0.001$; **Figure 4A**). Eye diameter at the limbus and axial length at day 14 demonstrated reasonable correlation to measures of IOP, indicating a relationship between the magnitudes of IOP increase and increase in the size of the eye (**Figure 4B-C**). There was no correlation between eye size and animal weight, confirming that animal age or size was not driving the observed difference (**Figure 4D**).

We reasoned that an increase in eye size may cause the retina to stretch, and as such, measurements of RGC density could be confounded, thus overestimating cell loss. Retinal length was variable in both NT (8.5 ± 0.8 mm) and OHT eyes (9.5 ± 1.0 mm), and no significant increase in retinal length was observed. RGC density (as an average across the whole retina) was significantly reduced in OHT eyes compared to NT eyes (57% decrease, $P < 0.001$; **Figure 4E**). RGC density was highly correlated with IOP measures and eye size (**Figure 4F**), whereas retinal length demonstrated more modest correlations (**Figure 4G**). Overall, these data demonstrate that globe expansion is a feature of the rat magnetic bead model. Although this does not result in significant retinal stretch, any analysis of RGC density (reported as percentage reduction relative to the contralateral eye) should take account of the variability in the retinal length and RGC numbers seen in both OHT and NT eyes. The observed decrease in blood vessel branching density and increase in lacunarity could also be explained by the changes to globe and retina size.

Retinal microglia demonstrate increasingly reactive morphologies in unilateral normotensive, unilateral ocular hypertensive, and bilateral ocular hypertensive eyes

We performed volume reconstructions of individual microglia (n = 1297 microglia; **Figure 5A-D**) and assessed branching complexity, field area, and volume. Individual microglia were binned by their position within the retinal layers to either nerve fibre layer/ganglion cell layer (NFL/GCL) or IPL microglia. Sholl analysis revealed a reduction in branching density (Sholl AUC) from NT/NT for NT/OHT, OHT/NT, and OHT/NT and with increasing magnitude of reduction through these groups (**Figure 5B**). This pattern of decrease was also observed in the number of branches, total process length, and field area of microglia (**Figure 5B**). Microglial volume increased in OHT eyes compared to NT eyes but there was no significant change in volume between NT/NT and NT/OHT eyes (**Figure 5B**). The data quantitatively demonstrate morphological changes consistent with activation (retraction and increased volume (40, 41)) occurring in microglia in OHT eyes. Microglia in NT eyes contralateral to OHT eyes demonstrate early reactive morphologies (retraction). In the IPL, microglial morphology largely followed the same trend (**Figure 5C-D**). Microglia from OHT eyes demonstrated significantly decreased Sholl AUC, number of branch points, total process length, and field area (**Figure 5D**). Microglial volume was increased in OHT eyes compared to NT eyes (**Figure 5D**). The contralateral response was more muted in IPL microglia with NT/NT and NT/OHT showing no significant difference in Sholl AUC, number of branch points, and total process length but significantly reduced field area and significantly increased volume (**Figure 5D**). OHT/OHT showed significant process retraction compared to OHT/NT but no significant increase in volume (**Figure 5D**), indicating that microglia in the IPL also display activated morphologies, that follow a similar pattern in magnitude of change (OHT/OHT > OHT/NT > NT/OHT > NT/NT), but to a lesser degree than microglia in the NFL/GCL.

We next performed hierarchical clustering (HC) of individual microglia in the NFL/GCL to determine whether these morphological measures alone could group microglia by degree of

activation (**Figure 6**). HC produced 4 clusters: Cluster 1; a small cluster, n =16, of NT/NT and NT/OHT microglia, Cluster 2; n = 210, predominantly consisting of NT/NT and NT/OHT microglia reflecting microglia with resting morphology (63.5% and 51.4 % of total NT/NT and NT/OHT respectively), Cluster 3; n = 156, a mix of microglia from all 4 groups, representing morphologies related to early activation, and Cluster 4; n = 359, predominantly OHT/NT and OHT/OHT microglia (67.5% and 85.6 % of total OHT/NT and OHT/OHT respectively), representing retracted and condensed morphologies consistent with activation (**Figure 6**).

Monocyte infiltration occurs early following ocular hypertension

Increased numbers of microglia in the retina have been reported following OHT, as have mild increases in microglia number in NT eyes contralateral to OHT eyes. Microglia density was increased in the NFL/GCL in both OHT/NT and OHT/OHT eyes compared to NT/NT (**Figure 7A**). There was no significantly detectable contralateral effect for either unilateral NT or OHT eyes in comparison to bilateral NT or OHT eyes (**Figure 7A**). Microglia density in the IPL was less variable between groups, with only OHT/NT eyes showing a significant increase over other groups (**Figure 7A**). NND analysis revealed that the distance between microglia in the NFL/GCL was smaller on average in OHT eyes than NT eyes, with no change in NT/OHT eyes compared to NT/NT eyes (**Figure 7B**). In the IPL, NND was also smaller between microglia in OHT eyes and in NT/OHT eyes compared to NT/NT eyes (**Figure 7B**). However, the interquartile range indicated that in the IPL the majority of NNDs for OHT eyes remained overlapping with those of NT eyes, whereas in the NFL/GCL these ranges were non-overlapping (**Figure 7B**). These data suggest that changes are modest in the IPL and that microglia here are largely distributed normally, but changes are more pronounced in the NFL/GCL. Given that microglial density was substantially increased (2.8 to 3.5-fold increase), NND was not increased to the same degree (1.6 to 2.4-fold increase) demonstrating that microglia remain well distributed (*i.e.* avoid clumping/clustering). The NND between microglia and RGCs significantly increased in microglia from both the NFL/GCL and IPL under OHT in comparison to NT (**Figure 7B**). Since the increase in microglial density was concurrent with the decrease in RGC density, these data suggest that microglia are not clustering around surviving RGCs.

Extravasation and increased monocyte infiltration has been demonstrated as an early and persistent feature of glaucoma in animal models (35) and in post-mortem human tissue (3), and $CD45^{hi}$ monocytes are present in the retina in low numbers under normal physiological conditions (42, 43). We observed Isolectin B4+ ameboid cells in the majority of retinas in all experimental groups but no significant change in average monocyte density across experimental groups (**Figure 7C**). NND analysis demonstrated a significant decrease in distance between monocytes in OHT eyes compared to NT eyes (all $P < 0.001$) and a substantial shift in the interquartile range, suggesting a clumping of monocytes that may reflect recruitment rather than random transient migration into the retina (**Figure 7C**). Monocyte infiltration has been shown to be an early event in glaucoma (35). We counted retinal myeloid-derived cells (MDCs) by flow cytometry at an early time-point

(3 days post-OHT induction, representing peak IOP in the absence of RGC death in our experimental groups; **Figure 7D**). Monocytes, but not microglia, were significantly increased at this early time-point in OHT compared to NT ($P < 0.01$; **Figure 7D**). This demonstrates early monocyte infiltration in the absence of microglial proliferation. This early increase in monocytes and a late increase in microglia supports a hypothesis in which infiltrating monocytes become monocyte derived microglia-like macrophages during glaucoma pathogenesis.

No detectable Müller glia activation following ocular hypertensive glaucoma

Müller glia provide trophic and metabolic support to RGCs during times of stress, including glaucoma related stresses (44, 45). Müller glia activation, identified by increased glutamine synthetase (GS) labelling, has been demonstrated in different animal models of glaucoma. To determine whether Müller glia activation was a component of glaucomatous neurodegeneration in this model, cryo-sections were labelled with antibodies targeting GS (**Figure 8A**). Analysis of GS labelling in the NFL/GCL/IPL (representing Müller glia association to RGC axon, soma, and dendrites) did not indicate significant Müller glial activation at this time point (**Figure 8B**).

Microglial activation extends into the optic nerve

Since RGC axonal loss with a concomitant loss of axon transport extended into the optic nerve in this model, we sought to determine whether this was accompanied by microglial activation. Microglia were assessed in longitudinal optic nerve sections (**Figure 9A**). Microglial counts demonstrated a significant increase in microglial density both proximal to the eye and proximal to the chiasm in OHT optic nerves compared to NT optic nerves (**Figure 9B**). No contralateral change was observed in microglial density in optic nerves (**Figure 9B**). Volume reconstructions of whole Isolectin B4 content demonstrated the same trend, with significant increases in OHT optic nerves compared to NT nerves, which was more pronounced proximal to the chiasm (**Figure 9B**). Microglial activation was most evidently demonstrated at the chiasm where RGC axons from unilateral OHT eyes decussate, with the appearance of activated microglia following both optic tracts post-chiasm (**Figure 9C**).

Microglia are activated in the dorsal lateral geniculate nucleus and superior colliculus in both hemispheres, irrespective of unilateral or bilateral ocular hypertension

Microglial activation in retinothalamic projections has been reported in animal models of glaucoma (21, 22). Brains were serial sectioned and microglia in central dLGN and SC were labelled (**Figure 10A-C**). Microglial activation was evident in the dLGN across both hemispheres in all conditions compared to brains from NT/NT animals. Microglia demonstrated reduced branching complexity, number of branch points, total process length, and field area, and an increased volume (**Figure 10D**). The dLGN contralateral to NT/OHT eyes (majority RGC input from NT eye) demonstrated significant changes in these measures compared to NT/NT dLGN, but not to its fellow dLGN (contralateral to OHT/NT eyes; **Figure 10D**), indicating that inflammation was not restricted, nor proportional, to the degree of RGC decussation. Microglia counts

demonstrated no significant increase in microglia density in the dLGN, suggesting activation in the absence of proliferation or infiltration (**Figure 10D**). In the SC, microglial morphology was also indicative of activation, with microglia demonstrating a significant reduction in branching complexity, number of branch points, total process length, and field area, and an increased volume in both hemispheres from all conditions compared to NT/NT (**Figure 10E**). In the SC, there was no significant difference in these measurements in microglia between hemispheres in unilateral animals, consistent with the findings in the dLGN (**Figure 10E**). Microglia from OHT/OHT animals and both hemispheres of the unilateral animals were more similar in morphology than in the retina (**Figure 10D-E**), suggesting that the degree of microglial activation in the brain is not contingent on the degree of dysfunctional and/or absent RGC input. Microglial density was increased in the SC in OHT/NT eyes, and highly variable in OHT/OHT eyes, suggesting proliferation or recruitment of microglia in the SC (**Figure 10E**). Since ameboid monocytes were not observed in either the SC or dLGN, and that the SC and dLGN are not directly insulted by elevated IOP, microglial proliferation is the most likely scenario. Both unilateral and bilateral OHT result in consistent microglial activation across both hemispheres of the visual thalami (*i.e.* neuroinflammatory signatures propagate even when only a small percentage of axons are damaged or dystrophic).

Upregulation of cytokines in ocular hypertension and in contralateral normotensive eyes

RGC dysfunction or neurodegeneration in the NT/OHT eyes, but with substantial microglial inflammation in the optic nerve and in terminal brain thalami, whole retinal lysate was probed for cytokine signals that could contribute to microglial activation (**Figure 11A**). Of the 79 analytes assessed by cytokine array, 6 were identified as significantly altered across groups by *MANOVA* (**Figure 11B-C**). These analytes were CNTF, Fetuin A, FGF-1, Galectin-3, ICAM-1 (CD54), and Lipocalin-2. OHT eyes demonstrated a significant upregulation of CNTF compared to NT eyes. Fetuin-A and ICAM-1 were significantly increased in OHT/NT eyes compared to NT/NT eyes (**Figure 11C**). Galectin-3 and Lipocalin-2 were significantly increased in OHT/OHT eyes compared to NT/NT eyes (**Figure 11C**). FGF-1 was significantly increased in NT/OHT eyes compared to NT/NT eyes (**Figure 11C**).

Discussion

Retinal ganglion cells are reliant on supportive glia throughout their long projections to terminal visual thalami (46). Following periods of elevated IOP these glia can become reactive, likely as an initial protective response that actually further compromises retinal ganglion cell survival (4, 47). Supporting this, complete ablation of microglia or monocytes only provides short-term neuroprotection in glaucoma (35, 48). In a recent study, almost complete depletion of resident microglia and infiltrating monocytes (using a PLX5622 and clodronate liposome combination treatment) failed to provide benefit in a more acute model (controlled optic nerve crush) and actually delayed axon regeneration following lens injury-induced RGC axon regeneration (49). In the present study, quantification of microglial morphology demonstrates retracted morphologies and increased process volume consistent with activation from a resting state (40, 41). Activated morphology persisted throughout the retina, optic nerve, and brain mirroring retinal ganglion cell dysfunction that extended along the trajectory of the axon. Reciprocal signalling between microglia and neurons plays an important role in defining microglia phenotypes (50). The resting, non-activated state, is in part controlled by CD200 and fractalkine (CX3CL1) signalling. CD200 is expressed by neurons and through binding CD200R on microglia, maintains a resting state (51, 52). CX3CL1 is expressed in neurons and can be membrane bound and in a secreted form; it signals through its receptor on microglia to maintain a resting state (53, 54). CD200 and CD200R expression changes early in glaucoma while loss of CX3CL1 signalling causes earlier axon transport dysfunction and in a DBA/2J mouse model of glaucoma (55, 56). Neurons also express markers of injury (*e.g.* surface expression of CCL21 which activates CXCR3 on microglia (52, 57, 58)) or of health (*e.g.* surface expression of CD47, the 'don't eat me' signal (59, 60)). Activated microglia exhibit increased expression of toll-like receptors, complement receptor and components, and pro-inflammatory cytokines and chemokines. Microglia and complement involvement in synapse elimination during the critical period and in neurodegenerative disease is well established (61-63). Complement components are upregulated in glaucoma in animal models and in human tissue, which play a critical involvement in synaptic pruning in glaucoma, and altered retinal ganglion cell survival through its manipulation (31, 33, 64-69). This reciprocal relationship between microglial activation and neuronal dysfunction may underlie why microglial activation is so robust in the SC and dLGN even in the absence of direct insult from OHT (*e.g.* direct IOP and vascular compromise).

The degree to which unilateral OHT affects the contralateral eye requires further elucidation. We confirmed quantitatively the observation of activated microglia in NT eyes contralateral to OHT eyes. In these eyes, as in the brain, activation occurs in the absence of direct OHT insult. The source of microglial insult is therefore either systemic or neuron-derived. We observed no significant change in IOP in NT/OHT eyes over NT/NT eyes (although NT/OHT eyes trended to have higher pressures but this did not reach significance). We also demonstrated no detectable (by gross histology) neurodegenerative effects in the retina in NT/OHT eyes. In the rat, decussation at

the chiasm of ~90% of axons to the SC and dLGN contralateral to the eye of origin leaves ~10% of RGC axons projecting ipsilaterally. Significant microglial activation therefore persists along a substantial portion of these retinal ganglion cell axons and presents a pro-neuroinflammatory environment to otherwise healthy RGC terminals. It is possible that this interaction translates into activation at the somal end in the retina, although this remains to be experimentally validated. Of note is the contralateral effect observed as the difference in activation between unilateral and bilateral OHT in the retina. This furthers the hypothesis that cumulative neuronal insult or systemic effects may drive activation to a greater degree in the retina. This graded effect in the retina was not observed in the brain, where microglial activation was consistent across hemispheres irrespective of whether the majority of input was from an OHT or NT eye in unilateral animals. The degree of microglial activation, and its implications towards neuro-glial signalling, neuroinflammatory environment, and RGC health should caution against the use of the contralateral eye as a control in unilateral OHT animals.

Microglial proliferation and migration and monocyte infiltration have been reported in a number of glaucoma models and in human glaucoma (3, 13, 35, 48, 56, 70-73). We demonstrate that an early increase in monocytes, but not microglia, and a late increase in microglia, but not monocytes occurs following sustained periods of OHT. These data suggest that monocytes infiltrate the retina and become microglia-like monocyte derived macrophages, as has been reported in Alzheimer's disease and other neurodegenerative diseases and in retinal photoreceptor degeneration (74-78). Definitively testing this hypothesis would require complex reporter alleles that are currently unavailable in the rat and therefore outside the scope of this study. We have previously shown that vascular permeability is compromised in glaucoma, leading to increased extravasation of monocytes in addition to recruitment through vascular endothelial changes (35, 73).

In our model, increased microglial activation and monocyte infiltration results in a significant pro-inflammatory environment. Cytokine and chemokine profiling in the retina identified a number of changes in OHT and in contralateral NT eyes. CNTF, Fetuin A, FGF-1, Galectin-3, ICAM-1 (CD54), and Lipocalin-2 were all differentially elevated. CNTF, which can be released from microglia as a response to central nervous system injury, has demonstrated neurotrophic properties and increases retinal ganglion cell survival in glaucoma models (79, 80). CNTF also induces gliosis in Müller cells and leads to upregulation of pro-inflammatory cytokines and chemokines (81-83), and as such its action is likely highly context dependant. Fetuin-A, a serum carrier protein, has been proposed as a biomarker of systemic inflammation, vascular disease, and neurodegenerative disease (84-86). Reduced expression of Fetuin-A correlates with the severity of cognitive impairment in Alzheimer's disease and Fetuin-A deficient mice demonstrate protection in experimental models of multiple sclerosis (87, 88). Galectin-3 mediates cell migration and adhesion, inflammatory cytokine release and apoptosis and has been shown to activate microglia, astrocytes, monocytes, and other immune cells (89). Plasma levels of Galectin-3 correlate with Huntington's disease severity in patients and animals, and are associated with adverse outcomes

in stroke and cerebral infarction (90, 91). Expression of Galectin-3 was increased in Huntington's disease and genetic ablation of *Lgals3* is protective in animal models (90). Microglial released Galectin-3 can act as a ligand for TLR4, sustaining inflammatory responses (92). Increased expression of Galectin-3 has been detected in human glaucomatous donor tissue in the trabecular meshwork and optic nerve head in association with increased fibrosis (93). Icam-1 is a glycoprotein that is expressed on leukocytes, macrophages and vascular endothelium. Its expression is upregulated in response to inflammatory stimuli (IL-1, TNF-α) where it functions as a ligand for integrins to facilitate endothelial binding and transmigration of leukocytes (94). *ICAM1* expression is increased in glaucoma patient leukocytes but not blood plasma (95, 96). The upregulation of *Icam1* is early and persistent in the optic nerve head and retina of DBA2/J mice, and is reduced by radiation treatment which is highly protective for retinal ganglion cells (48). Lipocalin-2 is an antibacterial protein (acting through iron-sequestration) that elicits pro-inflammatory responses and is implicated in a number of inflammatory and neurodegenerative diseases, including Stargardt disease and age-related macular degeneration in the retina (97, 98). *Lcn2* expression is also highly upregulated in DBA2/J glaucoma and in the rat hypertonic saline glaucoma model (48, 99). A recent GEO screen identified *LCN2* involvement in glaucoma pathogenesis (100). Increased FGF-1 expression was identified in NT/OHT eyes. FGF-1 has demonstrated neuroprotective responses in neurodegenerative disease, but also activates astrocytes in the spinal cord, leading to pro-inflammatory responses (101-104). Whether this represents a neuroprotective or inflammatory response related to microglial activation warrants further exploration. These pro-inflammatory molecules represent ideal candidates for further exploration using targeted knockouts, gene therapies, or antibody therapies in glaucoma.

Following periods of OHT, we identified global eye expansion as a feature of the paramagnetic bead model. While this is not a feature of adult glaucoma, it occurs in congenital glaucoma where the sclera is less rigid and more elastic (105, 106). Increased eye diameter and axial length was highly correlated to the magnitude and cumulative degree of IOP elevation. As the retina is fixed at the optic nerve and ora serrata, we reasoned that it may stretch with the eye globe. Retinal length was highly variable following OHT, and trended towards increase, but no significant change was detected. Global expansion should be considered when comparing to contralateral eyes, particularly if reporting percentage reductions to fellow eyes. Our data suggest caution is warranted when attributing findings comparatively to the contralateral 'control' eye, and these findings may, in part, help explain why many glaucoma therapies have failed in translation between rodents and humans.

Conclusions

In a rat glaucoma model we identify substantial microglial activation extending from the retina to visual thalami in combination with retinal ganglion cell degeneration. In unilateral OHT, activation of microglia occurs in the contralateral control eye and is substantial and comparable throughout

the visual thalami. Unilateral OHT animal models should be analysed with caution, particularly given the reciprocal signalling between neurons and immune cells in resting and pathogenic states.

List of abbreviations

AUC (area under the curve), FC (flow cytometry), GCL (ganglion cell layer), H&E (haematoxylin and eosin), HC (hierarchical clustering), IF (immunofluorescence), IHC (immunohistochemistry), IOP (intraocular pressure), IPL (inner plexiform layer), MDC (myeloid-derived cell), NND (nearest neighbour distance), NT (normotensive), NFL (nerve fibre layer), OHT (ocular hypertension).

Declarations

Ethics approval

All experimental procedures were undertaken in accordance with the Association for Research for Vision and Ophthalmology Statement for the Use of Animals in Ophthalmic and Research. Individual study protocols were approved by Stockholm's Committee for Ethical Animal Research (10389-2018).

Consent for publication

N/A

Availability of data and material

All data generated or analysed during this study are included in this published article.

Competing interests

The Authors report no competing interests.

Funding

Vetenskapsrådet 2018-02124 (PAW). Fight For Sight UK 512264 (JEM). Fight For Sight Denmark (MK). Pete Williams is supported by the Karolinska Institutet in the form of a Board of Research Faculty Funded Career Position and by St. Erik Eye Hospital philanthropic donations. Rupali Vohra is a part of the BRIDGE – Translational Excellence Programme at the Faculty of Health and Medical Sciences, University of Copenhagen (Novo Nordisk Foundation NNF18SA0034956).

Acknowledgments

The Authors would like to thank Monica Aronsson and Diana Rydholm for their assistance with animal husbandry and maintenance, St. Eriks Eye Hospital for financial support for research space, clinical histopathology, and animal facilities, the Knut and Alice Wallenberg Foundation and Karolinska Institutet for supporting the CLICK imaging facility, Annika van Vollenhoven at the Flow Cytometry Core Facility at the Karolinska Institutet Center for Molecular Medicine for flow cytometry, Charlotte Taul Brændstrup for assistance with Müller cell immunofluorescence, B Paul Morgan for critical reading and editing of the manuscript, and CITER (Cardiff Institute of Tissue Engineering & Repair) for supporting EK in the form of a research travel award.

Author contributions

JRT – designed and performed experiments, analysed data, wrote the manuscript; *EK* – designed and performed experiments, analysed data, wrote the manuscript; *AO* – performed experiments, analysed data; *FP* – performed experiments, analysed data; *EL* - performed experiments; *RV* – performed experiments; *MK* - provided resources, wrote the manuscript; *HA* - provided resources, designed experiments, wrote the manuscript; *JEM* – provided resources, designed experiments, wrote the manuscript; *PAW* – conceived, designed, performed experiments, analysed data, wrote the manuscript. All authors read and approved the final manuscript.

References

1. Tham YC, Li X, Wong TY, Quigley HA, Aung T, Cheng CY. Global prevalence of glaucoma and projections of glaucoma burden through 2040: a systematic review and meta-analysis. Ophthalmology. 2014;121(11):2081-90.
2. Peters D, Bengtsson B, Heijl A. Lifetime risk of blindness in open-angle glaucoma. Am J Ophthalmol. 2013;156(4):724-30.
3. Margeta MA, Lad EM, Proia AD. CD163+ macrophages infiltrate axon bundles of postmortem optic nerves with glaucoma. Graefes Arch Clin Exp Ophthalmol. 2018;256(12):2449-56.
4. Williams PA, Marsh-Armstrong N, Howell GR, Lasker IIA. Neuroinflammation in glaucoma: A new opportunity. Experimental Eye Research. 2017;157:20-7.
5. Cepurna WO, Kayton RJ, Johnson EC, Morrison JC. Age related optic nerve axonal loss in adult Brown Norway rats. Experimental Eye Research. 2005;80(6):877-84.
6. Dräger UC, Olsen JF. Origins of crossed and uncrossed retinal projections in pigmented and albino mice. J Comp Neurol. 1980;191(3):383-412.
7. Jeffery G, Thompson ID. The effects of prenatal and neonatal monocular enucleation on visual topography in the uncrossed retinal pathway to the Rat superior colliculus. Experimental Brain Research. 1986;63(2):351-63.
8. Fukuda Y, Sawai H, Watanabe M, Wakakuwa K, Morigiwa K. Nasotemporal overlap of crossed and uncrossed retinal ganglion cell projections in the Japanese monkey (Macaca fuscata). J Neurosci. 1989;9(7):2353-73.
9. Balkema GW, Pinto LH, Dräger UC, Vanable JW. Characterization of abnormalities in the visual system of the mutant mouse pearl. J Neurosci. 1981;1(11):1320-9.
10. Ahmed AK, Guison NG, Yamadori T. A retrograde fluorescent-labeling study of direct relationship between the limbic (anterodorsal and anteroventral thalamic nuclei) and the visual system in the albino rat. Brain Res. 1996;729(1):119-23.
11. Dreher B, Sefton AJ, Ni SY, Nisbett G. The morphology, number, distribution and central projections of Class I retinal ganglion cells in albino and hooded rats. Brain Behav Evol. 1985;26(1):10-48.
12. Lund RD. Uncrossed Visual Pathways of Hooded and Albino Rats. Science. 1965;149(3691):1506-7.
13. Bosco A, Steele MR, Vetter ML. Early Microglia Activation in a Mouse Model of Chronic Glaucoma. Journal of Comparative Neurology. 2011;519(4):599-620.
14. Qu J, Jakobs TC. The Time Course of Gene Expression during Reactive Gliosis in the Optic Nerve. PLoS One. 2013;8(6):e67094.
15. Ebneter A, Casson RJ, Wood JP, Chidlow G. Microglial activation in the visual pathway in experimental glaucoma: spatiotemporal characterization and correlation with axonal injury. Invest Ophthalmol Vis Sci. 2010;51(12):6448-60.
16. Neufeld AH. Microglia in the optic nerve head and the region of parapapillary chorioretinal atrophy in glaucoma. Archives of Ophthalmology. 1999;117(8):1050-6.
17. Yuan L, Neufeld AH. Activated microglia in the human glaucomatous optic nerve head. J Neurosci Res. 2001;64(5):523-32.
18. Gallego BI, Salazar JJ, de Hoz R, Rojas B, Ramírez AI, Salinas-Navarro M, et al. IOP induces upregulation of GFAP and MHC-II and microglia reactivity in mice retina contralateral to experimental glaucoma. J Neuroinflammation. 2012;9:92.

19. Rojas B, Gallego BI, Ramirez AI, Salazar JJ, de Hoz R, Valiente-Soriano FJ, et al. Microglia in mouse retina contralateral to experimental glaucoma exhibit multiple signs of activation in all retinal layers. Journal of Neuroinflammation. 2014;11.
20. Kezic JM, Chrysostomou V, Trounce IA, McMenamin PG, Crowston JG. Effect of anterior chamber cannulation and acute IOP elevation on retinal macrophages in the adult mouse. Invest Ophthalmol Vis Sci. 2013;54(4):3028-36.
21. Sapienza A, Raveu AL, Reboussin E, Roubeix C, Boucher C, Dégardin J, et al. Bilateral neuroinflammatory processes in visual pathways induced by unilateral ocular hypertension in the rat. J Neuroinflammation. 2016;13:44.
22. Wang X, Sam-Wah Tay S, Ng YK. Nitric oxide, microglial activities and neuronal cell death in the lateral geniculate nucleus of glaucomatous rats. Brain Res. 2000;878(1-2):136-47.
23. Samsel PA, Kisiswa L, Erichsen JT, Cross SD, Morgan JE. A Novel Method for the Induction of Experimental Glaucoma Using Magnetic Microspheres. Investigative Ophthalmology & Visual Science. 2011;52(3):1671-5.
24. Morgan JE, Tribble JR. Microbead models in glaucoma. Experimental Eye Research. 2015;141:9-14.
25. Schindelin J, Arganda-Carreras I, Frise E, Kaynig V, Longair M, Pietzsch T, et al. Fiji: an open-source platform for biological-image analysis. Nat Methods. 2012;9(7):676-82.
26. Preibisch S, Saalfeld S, Tomancak P. Globally optimal stitching of tiled 3D microscopic image acquisitions. Bioinformatics. 2009;25(11):1463-5.
27. Zudaire E, Gambardella L, Kurcz C, Vermeren S. A computational tool for quantitative analysis of vascular networks. PLoS One. 2011;6(11):e27385.
28. Groemping U. Relative Importance for Linear Regression in R: The Package relaimpo. Journal of Statistical Software. 2006;1.
29. Baddeley A, Rubak E, Turner R. Spatial Point Patterns: Methodology and Applications with R. 1st Edition ed: Chapman and Hall/CRC; 2015.
30. Rezakhaniha R, Agianniotis A, Schrauwen JT, Griffa A, Sage D, Bouten CV, et al. Experimental investigation of collagen waviness and orientation in the arterial adventitia using confocal laser scanning microscopy. Biomech Model Mechanobiol. 2012;11(3-4):461-73.
31. Williams PA, Tribble JR, Pepper KW, Cross SD, Morgan BP, Morgan JE, et al. Inhibition of the classical pathway of the complement cascade prevents early dendritic and synaptic degeneration in glaucoma. Molecular Neurodegeneration. 2016;11.
32. Tribble JR, Williams PA, Caterson B, Sengpiel F, Morgan JE. Digestion of the glycosaminoglycan extracellular matrix by chondroitinase ABC supports retinal ganglion cell dendritic preservation in a rodent model of experimental glaucoma. Mol Brain. 2018;11(1):69.
33. Howell GR, Macalinao DG, Sousa GL, Walden M, Soto I, Kneeland SC, et al. Molecular clustering identifies complement and endothelin induction as early events in a mouse model of glaucoma. Journal of Clinical Investigation. 2011;121(4):1429-44.
34. Howell GR, MacNicoll KH, Braine CE, Soto I, Macalinao DG, Sousa GL, et al. Combinatorial targeting of early pathways profoundly inhibits neurodegeneration in a mouse model of glaucoma. Neurobiol Dis. 2014;71:44-52.
35. Williams PA, Braine CE, Kizhatil K, Foxworth NE, Tolman NG, Harder JM, et al. Inhibition of monocyte-like cell extravasation protects from neurodegeneration in DBA/2J glaucoma. Mol Neurodegener. 2019;14(1):6.
36. Chung HS, Harris A, Kagemann L, Martin B. Peripapillary retinal blood flow in normal tension glaucoma. Br J Ophthalmol. 1999;83(4):466-9.

37. Whitmore AV, Libby RT, John SWM. Glaucoma: Thinking in new ways - a role for autonomous axonal self-destruction and other compartmentalised processes? Progress in Retinal and Eye Research. 2005;24(6):639-62.
38. Lye-Barthel M, Sun D, Jakobs TC. Morphology of astrocytes in a glaucomatous optic nerve. Invest Ophthalmol Vis Sci. 2013;54(2):909-17.
39. Liu B, Neufeld AH. Expression of nitric oxide synthase-2 (NOS-2) in reactive astrocytes of the human glaucomatous optic nerve head. Glia. 2000;30(2):178-86.
40. Stence N, Waite M, Dailey ME. Dynamics of microglial activation: a confocal time-lapse analysis in hippocampal slices. Glia. 2001;33(3):256-66.
41. Ransohoff RM, Perry VH. Microglial physiology: unique stimuli, specialized responses. Annu Rev Immunol. 2009;27:119-45.
42. Paschalis EI, Lei F, Zhou C, Kapoulea V, Dana R, Chodosh J, et al. Permanent neuroglial remodeling of the retina following infiltration of CSF1R inhibition-resistant peripheral monocytes. Proc Natl Acad Sci U S A. 2018;115(48):E11359-E68.
43. Karlen SJ, Miller EB, Wang X, Levine ES, Zawadzki RJ, Burns ME. Monocyte infiltration rather than microglia proliferation dominates the early immune response to rapid photoreceptor degeneration. J Neuroinflammation. 2018;15(1):344.
44. Vohra R, Aldana BI, Skytt DM, Freude K, Waagepetersen H, Bergersen LH, et al. Essential Roles of Lactate in Müller Cell Survival and Function. Mol Neurobiol. 2018;55(12):9108-21.
45. Skytt DM, Toft-Kehler AK, Brændstrup CT, Cejvanovic S, Gurubaran IS, Bergersen LH, et al. Glia-Neuron Interactions in the Retina Can Be Studied in Cocultures of Müller Cells and Retinal Ganglion Cells. Biomed Res Int. 2016;2016:1087647.
46. Vecino E, Rodriguez FD, Ruzafa N, Pereiro X, Sharma SC. Glia-neuron interactions in the mammalian retina. Prog Retin Eye Res. 2016;51:1-40.
47. Zeng HL, Shi JM. The role of microglia in the progression of glaucomatous neurodegeneration- a review. Int J Ophthalmol. 2018;11(1):143-9.
48. Howell GR, Soto I, Zhu X, Ryan M, Macalinao DG, Sousa GL, et al. Radiation treatment inhibits monocyte entry into the optic nerve head and prevents neuronal damage in a mouse model of glaucoma. Journal of Clinical Investigation. 2012;122(4):1246-61.
49. Hilla AM, Diekmann H, Fischer D. Microglia Are Irrelevant for Neuronal Degeneration and Axon Regeneration after Acute Injury. J Neurosci. 2017;37(25):6113-24.
50. Szepesi Z, Manouchehrian O, Bachiller S, Deierborg T. Bidirectional Microglia-Neuron Communication in Health and Disease. Front Cell Neurosci. 2018;12:323.
51. Hoek RM, Ruuls SR, Murphy CA, Wright GJ, Goddard R, Zurawski SM, et al. Down-regulation of the macrophage lineage through interaction with OX2 (CD200). Science. 2000;290(5497):1768-71.
52. Biber K, Sauter A, Brouwer N, Copray SC, Boddeke HW. Ischemia-induced neuronal expression of the microglia attracting chemokine Secondary Lymphoid-tissue Chemokine (SLC). Glia. 2001;34(2):121-33.
53. Nishiyori A, Minami M, Ohtani Y, Takami S, Yamamoto J, Kawaguchi N, et al. Localization of fractalkine and CX3CR1 mRNAs in rat brain: does fractalkine play a role in signaling from neuron to microglia? FEBS Lett. 1998;429(2):167-72.
54. Maciejewski-Lenoir D, Chen S, Feng L, Maki R, Bacon KB. Characterization of fractalkine in rat brain cells: migratory and activation signals for CX3CR-1-expressing microglia. J Immunol. 1999;163(3):1628-35.

55. Taylor S, Calder CJ, Albon J, Erichsen JT, Boulton ME, Morgan JE. Involvement of the CD200 receptor complex in microglia activation in experimental glaucoma. Experimental Eye Research. 2011;92(5).
56. Breen KT, Anderson SR, Steele MR, Calkins DJ, Bosco A, Vetter ML. Loss of Fractalkine Signaling Exacerbates Axon Transport Dysfunction in a Chronic Model of Glaucoma. Front Neurosci. 2016;10:526.
57. Dijkstra IM, Hulshof S, van der Valk P, Boddeke HW, Biber K. Cutting edge: activity of human adult microglia in response to CC chemokine ligand 21. J Immunol. 2004;172(5):2744-7.
58. van Weering HR, de Jong AP, de Haas AH, Biber KP, Boddeke HW. CCL21-induced calcium transients and proliferation in primary mouse astrocytes: CXCR3-dependent and independent responses. Brain Behav Immun. 2010;24(5):768-75.
59. Lehrman EK, Wilton DK, Litvina EY, Welsh CA, Chang ST, Frouin A, et al. CD47 Protects Synapses from Excess Microglia-Mediated Pruning during Development. Neuron. 2018;100(1):120-34.e6.
60. van Beek EM, Cochrane F, Barclay AN, van den Berg TK. Signal regulatory proteins in the immune system. J Immunol. 2005;175(12):7781-7.
61. Stevens B, Allen NJ, Vazquez LE, Howell GR, Christopherson KS, Nouri N, et al. The classical complement cascade mediates CNS synapse elimination. Cell. 2007;131(6):1164-78.
62. Schafer DP, Lehrman EK, Kautzman AG, Koyama R, Mardinly AR, Yamasaki R, et al. Microglia sculpt postnatal neural circuits in an activity and complement-dependent manner. Neuron. 2012;74(4):691-705.
63. Rajendran L, Paolicelli RC. Microglia-Mediated Synapse Loss in Alzheimer's Disease. J Neurosci. 2018;38(12):2911-9.
64. Miyahara T, Kikuchi T, Akimoto M, Kurokawa T, Shibuki H, Yoshimura N. Gene microarray analysis of experimental glaucomatous retina from cynomologous monkey. Invest Ophthalmol Vis Sci. 2003;44(10):4347-56.
65. Kuehn MH, Kim CY, Ostojic J, Bellin M, Alward WLM, Stone EM, et al. Retinal synthesis and deposition of complement components induced by ocular hypertension. Experimental Eye Research. 2006;83(3):620-8.
66. Tezel G, Yang X, Luo C, Kain AD, Powell DW, Kuehn MH, et al. Oxidative Stress and the Regulation of Complement Activation in Human Glaucoma. Investigative Ophthalmology & Visual Science. 2010;51(10):5071-82.
67. Harder JM, Braine CE, Williams PA, Zhu X, MacNicoll KH, Sousa GL, et al. Early immune responses are independent of RGC dysfunction in glaucoma with complement component C3 being protective. Proc Natl Acad Sci U S A. 2017;114(19):E3839-E48.
68. Bosco A, Anderson SR, Breen KT, Romero CO, Steele MR, Chiodo VA, et al. Complement C3-Targeted Gene Therapy Restricts Onset and Progression of Neurodegeneration in Chronic Mouse Glaucoma. Mol Ther. 2018;26(10):2379-96.
69. Howell GR, Soto I, Ryan M, Graham LC, Smith RS, John SWM. Deficiency of complement component 5 ameliorates glaucoma in DBA/2J mice. Journal of Neuroinflammation. 2013;10.
70. Gallego BI, Salazar JJ, de Hoz R, Rojas B, Ramirez AI, Salinas-Navarro M, et al. IOP induces upregulation of GFAP and MHC-II and microglia reactivity in mice retina contralateral to experimental glaucoma. Journal of Neuroinflammation. 2012;9.

71. Rojas B, Gallego BI, Ramírez AI, Salazar JJ, de Hoz R, Valiente-Soriano FJ, et al. Microglia in mouse retina contralateral to experimental glaucoma exhibit multiple signs of activation in all retinal layers. J Neuroinflammation. 2014;11:133.
72. Joachim SC, Gramlich OW, Laspas P, Schmid H, Beck S, von Pein HD, et al. Retinal Ganglion Cell Loss Is Accompanied by Antibody Depositions and Increased Levels of Microglia after Immunization with Retinal Antigens. Plos One. 2012;7(7).
73. Williams PA, Braine CE, Foxworth NE, Cochran KE, John SWM. GlyCAM1 negatively regulates monocyte entry into the optic nerve head and contributes to radiation-based protection in glaucoma. J Neuroinflammation. 2017;14(1):93.
74. Fani Maleki A, Rivest S. Innate Immune Cells: Monocytes, Monocyte-Derived Macrophages and Microglia as Therapeutic Targets for Alzheimer's Disease and Multiple Sclerosis. Front Cell Neurosci. 2019;13:355.
75. Thériault P, ElAli A, Rivest S. The dynamics of monocytes and microglia in Alzheimer's disease. Alzheimers Res Ther. 2015;7(1):41.
76. Lund H, Pieber M, Parsa R, Han J, Grommisch D, Ewing E, et al. Competitive repopulation of an empty microglial niche yields functionally distinct subsets of microglia-like cells. Nat Commun. 2018;9(1):4845.
77. Ronning KE, Karlen SJ, Miller EB, Burns ME. Molecular profiling of resident and infiltrating mononuclear phagocytes during rapid adult retinal degeneration using single-cell RNA sequencing. Sci Rep. 2019;9(1):4858.
78. Ma W, Zhang Y, Gao C, Fariss RN, Tam J, Wong WT. Monocyte infiltration and proliferation reestablish myeloid cell homeostasis in the mouse retina following retinal pigment epithelial cell injury. Sci Rep. 2017;7(1):8433.
79. Ji JZ, Elyaman W, Yip HK, Lee VW, Yick LW, Hugon J, et al. CNTF promotes survival of retinal ganglion cells after induction of ocular hypertension in rats: the possible involvement of STAT3 pathway. Eur J Neurosci. 2004;19(2):265-72.
80. Pease ME, Zack DJ, Berlinicke C, Bloom K, Cone F, Wang Y, et al. Effect of CNTF on retinal ganglion cell survival in experimental glaucoma. Invest Ophthalmol Vis Sci. 2009;50(5):2194-200.
81. Xue W, Cojocaru RI, Dudley VJ, Brooks M, Swaroop A, Sarthy VP. Ciliary neurotrophic factor induces genes associated with inflammation and gliosis in the retina: a gene profiling study of flow-sorted, Müller cells. PLoS One. 2011;6(5):e20326.
82. Lin HW, Jain MR, Li H, Levison SW. Ciliary neurotrophic factor (CNTF) plus soluble CNTF receptor alpha increases cyclooxygenase-2 expression, PGE2 release and interferon-gamma-induced CD40 in murine microglia. J Neuroinflammation. 2009;6:7.
83. Kahn MA, Ellison JA, Speight GJ, de Vellis J. CNTF regulation of astrogliosis and the activation of microglia in the developing rat central nervous system. Brain Res. 1995;685(1-2):55-67.
84. Guo VY, Cao B, Cai C, Cheng KK, Cheung BMY. Fetuin-A levels and risk of type 2 diabetes mellitus: a systematic review and meta-analysis. Acta Diabetol. 2018;55(1):87-98.
85. Naito C, Hashimoto M, Watanabe K, Shirai R, Takahashi Y, Kojima M, et al. Facilitatory effects of fetuin-A on atherosclerosis. Atherosclerosis. 2016;246:344-51.
86. Jirak P, Stechemesser L, Moré E, Franzen M, Topf A, Mirna M, et al. Clinical implications of fetuin-A. Adv Clin Chem. 2019;89:79-130.

87. Smith ER, Nilforooshan R, Weaving G, Tabet N. Plasma fetuin-A is associated with the severity of cognitive impairment in mild-to-moderate Alzheimer's disease. J Alzheimers Dis. 2011;24(2):327-33.
88. Harris VK, Donelan N, Yan QJ, Clark K, Touray A, Rammal M, et al. Cerebrospinal fluid fetuin-A is a biomarker of active multiple sclerosis. Mult Scler. 2013;19(11):1462-72.
89. Arikawa T, Simamura E, Shimada H, Nakamura T, Hatta T, Shoji H. Significance of sugar chain recognition by galectins and its involvement in disease-associated glycosylation. Congenit Anom (Kyoto). 2014;54(2):77-81.
90. Siew JJ, Chen HM, Chen HY, Chen HL, Chen CM, Soong BW, et al. Galectin-3 is required for the microglia-mediated brain inflammation in a model of Huntington's disease. Nat Commun. 2019;10(1):3473.
91. Nishikawa H, Suzuki H. Possible Role of Inflammation and Galectin-3 in Brain Injury after Subarachnoid Hemorrhage. Brain Sci. 2018;8(2).
92. Burguillos MA, Svensson M, Schulte T, Boza-Serrano A, Garcia-Quintanilla A, Kavanagh E, et al. Microglia-Secreted Galectin-3 Acts as a Toll-like Receptor 4 Ligand and Contributes to Microglial Activation. Cell Rep. 2015;10(9):1626-38.
93. Belmares R, Raychaudhuri U, Maansson S, Clark AF. Histological investigation of human glaucomatous eyes: Extracellular fibrotic changes and galectin 3 expression in the trabecular meshwork and optic nerve head. Clin Anat. 2018;31(7):1031-49.
94. Williams MR, Luscinskas FW. Leukocyte rolling and adhesion via ICAM-1 signals to endothelial permeability. Focus on "Leukocyte rolling and adhesion both contribute to regulation of microvascular permeability to albumin via ligation of ICAM-1". Am J Physiol Cell Physiol. 2011;301(4):C777-9.
95. Yeghiazaryan K, Flammer J, Orgül S, Wunderlich K, Golubnitschaja O. Vasospastic individuals demonstrate significant similarity to glaucoma patients as revealed by gene expression profiling in circulating leukocytes. Mol Vis. 2009;15:2339-48.
96. Kang JH, Wiggs JL, Pasquale LR. A nested case control study of plasma ICAM-1, E-selectin and TNF receptor 2 levels, and incident primary open-angle glaucoma. Invest Ophthalmol Vis Sci. 2013;54(3):1797-804.
97. Jha MK, Lee S, Park DH, Kook H, Park KG, Lee IK, et al. Diverse functional roles of lipocalin-2 in the central nervous system. Neurosci Biobehav Rev. 2015;49:135-56.
98. Parmar T, Parmar VM, Perusek L, Georges A, Takahashi M, Crabb JW, et al. Lipocalin 2 Plays an Important Role in Regulating Inflammation in Retinal Degeneration. J Immunol. 2018;200(9):3128-41.
99. Ahmed F, Brown KM, Stephan DA, Morrison JC, Johnson EC, Tomarev SI. Microarray analysis of changes in mRNA levels in the rat retina after experimental elevation of intraocular pressure. Invest Ophthalmol Vis Sci. 2004;45(4):1247-58.
100. Feng J, Xu J. Identification of pathogenic genes and transcription factors in glaucoma. Mol Med Rep. 2019;20(1):216-24.
101. Wei X, He S, Wang Z, Wu J, Zhang J, Cheng Y, et al. Fibroblast growth factor 1attenuates 6-hydroxydopamine-induced neurotoxicity: an in vitro and in vivo investigation in experimental models of parkinson's disease. Am J Transl Res. 2014;6(6):664-77.
102. Guo ZH, Mattson MP. Neurotrophic factors protect cortical synaptic terminals against amyloid and oxidative stress-induced impairment of glucose transport, glutamate transport and mitochondrial function. Cereb Cortex. 2000;10(1):50-7.

103. Thorns V, Masliah E. Evidence for neuroprotective effects of acidic fibroblast growth factor in Alzheimer disease. J Neuropathol Exp Neurol. 1999;58(3):296-306.
104. Garré JM, Yang G, Bukauskas FF, Bennett MV. FGF-1 Triggers Pannexin-1 Hemichannel Opening in Spinal Astrocytes of Rodents and Promotes Inflammatory Responses in Acute Spinal Cord Slices. J Neurosci. 2016;36(17):4785-801.
105. Terraciano AJ, Sidoti PA. Management of refractory glaucoma in childhood. Curr Opin Ophthalmol. 2002;13(2):97-102.
106. Stowell C, Burgoyne CF, Tamm ER, Ethier CR, Participants LIIoAaGN. Biomechanical aspects of axonal damage in glaucoma: A brief review. Exp Eye Res. 2017;157:13-9.

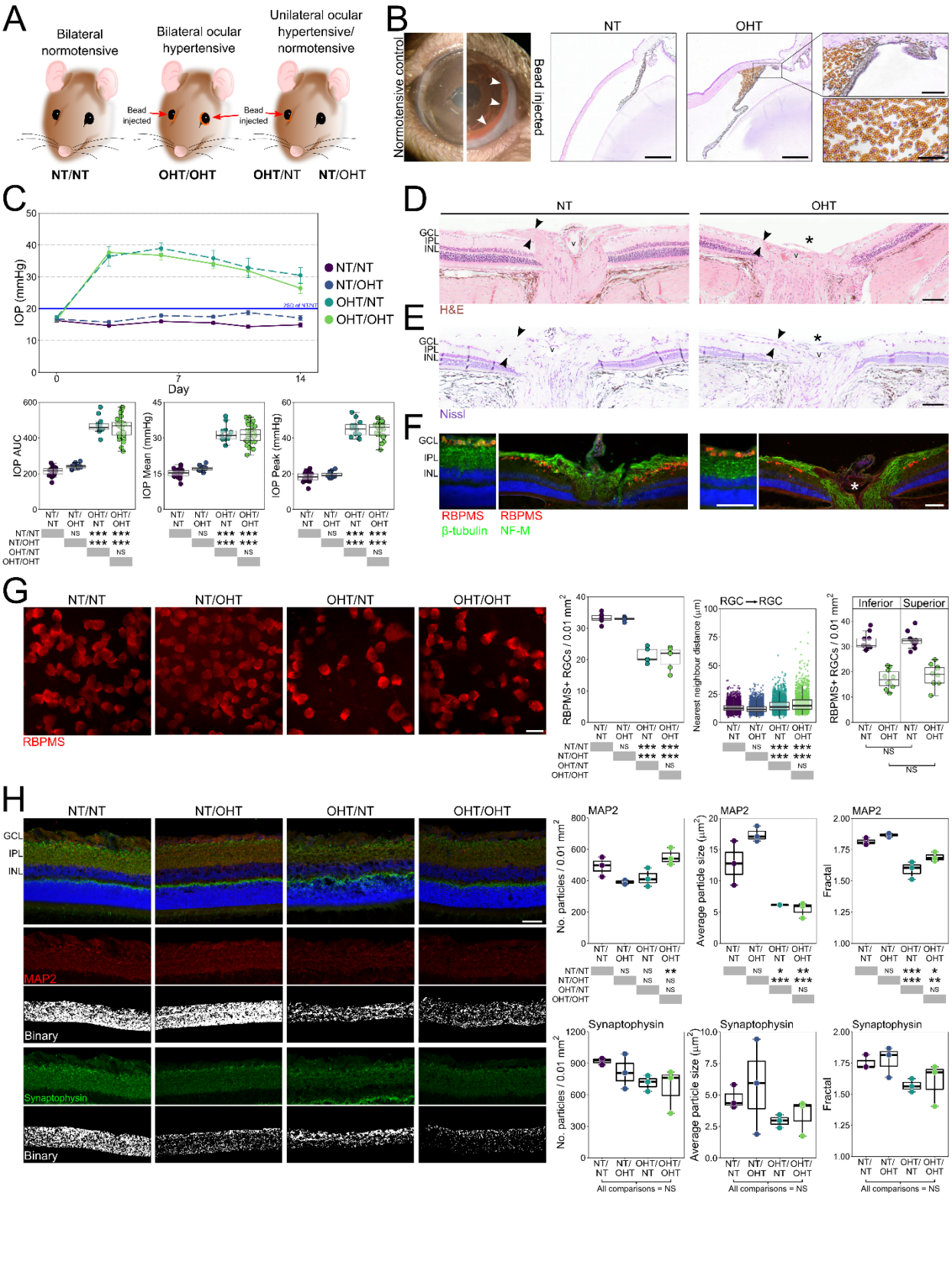
A
Bilateral normotensive
Bilateral ocular hypertensive
Unilateral ocular hypertensive/ normotensive
Bead injected
Bead injected
NT/NT
OHT/OHT
OHT/NT
NT/OHT
B
Normotensive control
Bead injected
NT
OHT
C
IOP (mmHg)
Day
NT/NT
NT/OHT
OHT/NT
OHT/OHT
IOP AUC
IOP Mean (mmHg)
IOP Peak (mmHg)
D
NT
OHT
GCL
IPL
INL
H&E
E
Nissl
F
RBPMS
β-tubulin
RBPMS
NF-M
G
NT/NT
NT/OHT
OHT/NT
OHT/OHT
RBPMS
RBPMS+ RGCs / 0.01 mm²
Nearest neighbour distance (µm)
RGC → RGC
Inferior
Superior
H
MAP2
Binary
Synaptophysin
No. particles / 0.01 mm²
Average particle size (µm²)
Fractal
All comparisons = NS

Figure 1: Induction of OHT via paramagnetic bead induction. (**A**) Brown Norway rats underwent intracameral injections of paramagnetic beads either bilaterally or unilaterally. The contralateral eye remained un-operated. (**B**) Beads were pulled into the drainage structures of the eye via a rare earth magnet (5 mm tip) (*left panel*). Histology (*right panels and insets*) demonstrate that beads remained within the drainage structures of the trabecular meshwork and Schlemm's canal. This resulted in significant and robust IOP increase that was sustained until euthanasia (**C**). 14 days of OHT results in significant RGC atrophy, axon degeneration and nerve fibre layer thinning (black arrows at the optic nerve head), and optic nerve excavation (*). Inner retinal degeneration is shown through 2 modalities; H&E staining (**D**), Nissl staining (**E**), and immunofluorescence for antibodies against RGC specific markers (RBPMS, β-tubulin, NF-M) (**F**). (**G**) RGC populations were assessed in flat-mount retinas confirming a significant loss of RGCs and increased NND of RGCs following 14 days OHT. There was no detectable region specific loss between superior and inferior retina. (**H**) OHT also resulted in significant dendritic atrophy (MAP2 labelling) but without a gross loss of synapses (synaptophysin labelling). A reduction in average particle size and a reduction in fractal indicates increased fragmentation and reduced space filling of dendrites in the IPL, which is suggestive of dendritic atrophy and retraction. For complete *n* please see **Methods**. Scale bars = 500 µm in **B** (*right panels*), 100 µm in **B** (*right inset, upper*), 50 µm in **B** (*right inset, lower*), 100 µm in **D**, **E** and **F**, 20 µm in **G**, 50 µm in **H** * = $P < 0.05$, ** = $P < 0.01$, *** $P < 0.001$, NS = non-significant ($P > 0.05$).

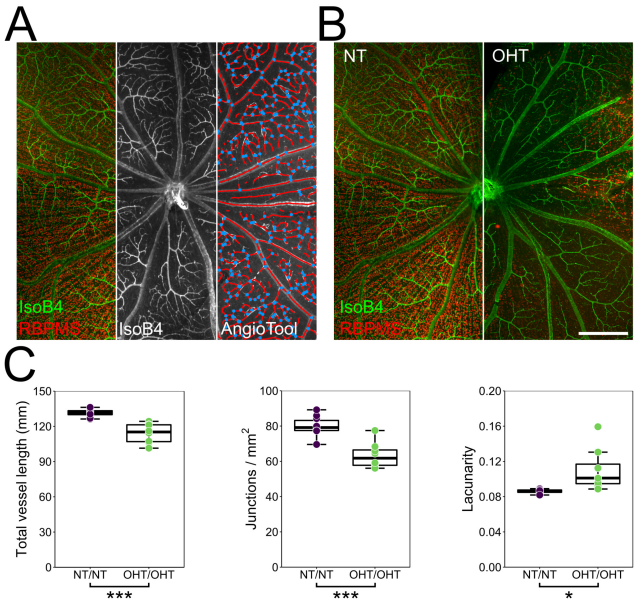

Figure 2: Vascular remodelling following OHT. (**A**) Flat-mounted retinas were labelled with Isolectin B4 and the inner retina imaged to assess blood vessel morphology. Blood vessels were reconstructed with AngioTool (**A**, right panel; vessels = red, junctions = blue). (**B-C**) Following OHT there was significant vascular remodelling assessed by a decrease in total vessel length and number of vessel junctions and an increase in lacunarity indicting reduced vessel coverage of the inner retina. Lacunarity is a measure of space filling within the image, where a high lacunarity equals less space filling by blood vessels. Scale bar = 500 µm in **B**, * = $P < 0.05$, ** = $P < 0.01$, *** $P < 0.001$, NS = non-significant ($P > 0.05$).

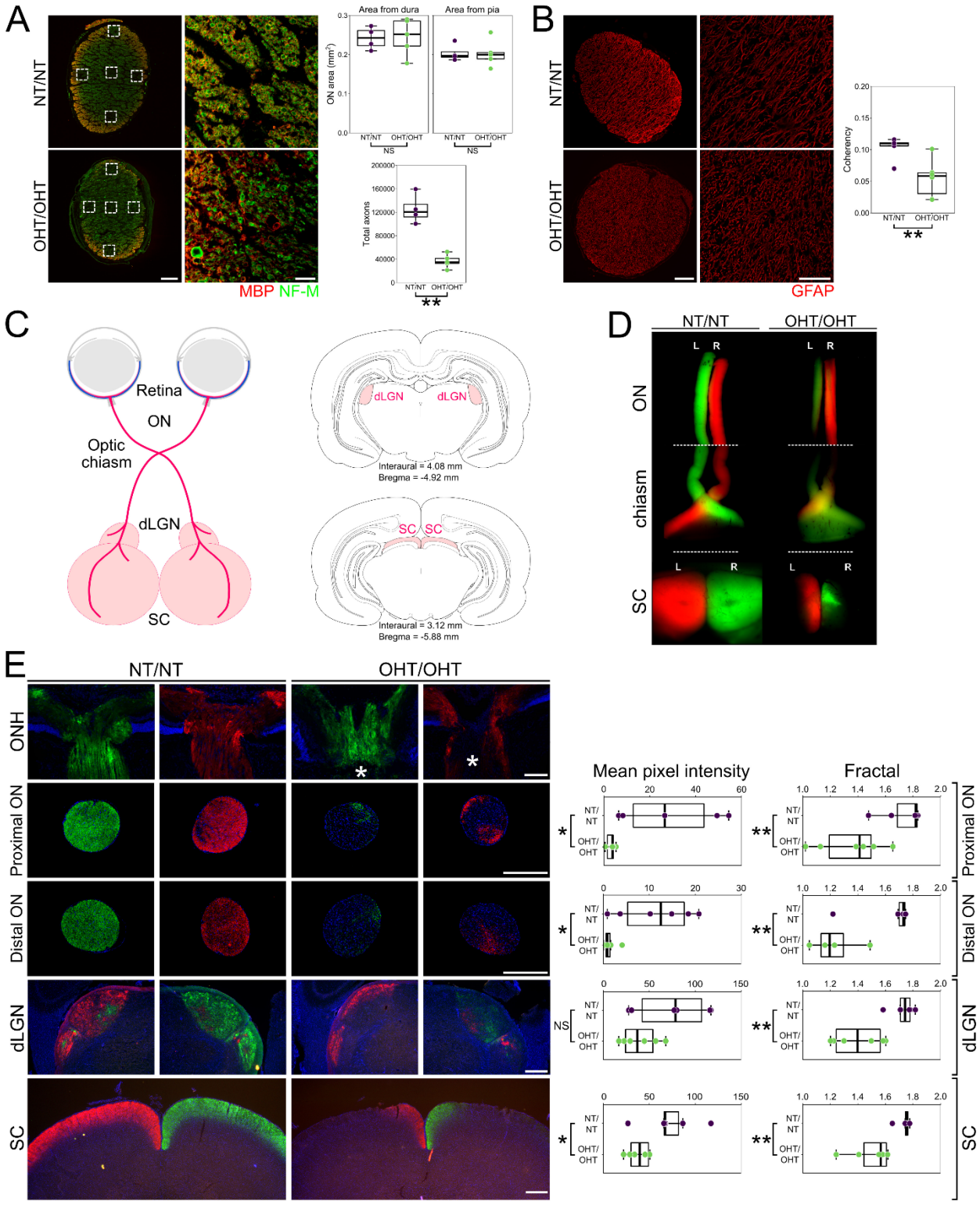
A
NT/NT
OHT/OHT
MBP NF-M
Area from dura
Area from pia
ON area (mm²)
NT/NT
OHT/OHT
NS
Total axons
**
B
GFAP
Coherency
C
Retina
ON
Optic chiasm
dLGN
SC
Interaural = 4.08 mm
Bregma = -4.92 mm
Interaural = 3.12 mm
Bregma = -5.88 mm
D
L
R
ON
chiasm
SC
E
ONH
Proximal ON
Distal ON
dLGN
Mean pixel intensity
Fractal
NT/NT
OHT/OHT
*
**
NS

Figure 3: OHT results in axon degeneration and deficits in axoplasmic transport. (**A**) Total axon number was assessed in optic nerve sections by high resolution imaging of NF-M+ axon fibres and myelin bundles (myelin basic protein; MBP). The estimated total number of axons in NT optic nerves (average 125,000) matched those reported in the literature for adult Brown Norway rats (5) and was significantly reduced in OHT eyes. The reduction is likely an overestimate due to an increased number of dystrophic axons in OHT optic nerves that may mask individual small calibre axons. There were no gross changes to optic nerve total size (as measured from the dura or pia mater) but a significant loss of RGC axons. (**B**) OHT results in significant remodelling of optic nerve astrocytes (a decrease in fibre alignment and coherency as assessed by OrientationJ). Axoplasmic transport was assessed by 2-color CT-β tracing from the retina to the terminal visual thalami (dLGN and SC). A schematic showing RGC trajectories and visual thalami is shown in (**C**). OHT results in an absence of axoplasmic transport to terminal regions assessed by both low power flat-mount SCs (**D**) and in cryo-sections (**E**) as assessed by mean pixel intensity and fractal analysis. Axoplasmic transport was primarily stalled within the optic nerve head (* in **E**) resulting in partial transport through the optic nerve to the dLGN and SC. Optic nerves were assessed both proximal to the eye and proximal to the chiasm. The dLGN and SC were assessed in 3 sections representing rostral, medial, and caudal dLGN or SC respectively. ONH = optic nerve head, ON = optic nerve. Scale bars = 100 µm in **A** (*left panels*), 10 µm in **A** (*right insets*), 100 µm in **B** (*left panels*), 50 µm in **B** (*right insets*), 100 µm in **E** (ONH), 500 µm in **E** (ON, dLGN, SC), * = $P < 0.05$, ** = $P < 0.01$, *** $P < 0.001$, NS = non-significant ($P > 0.05$).

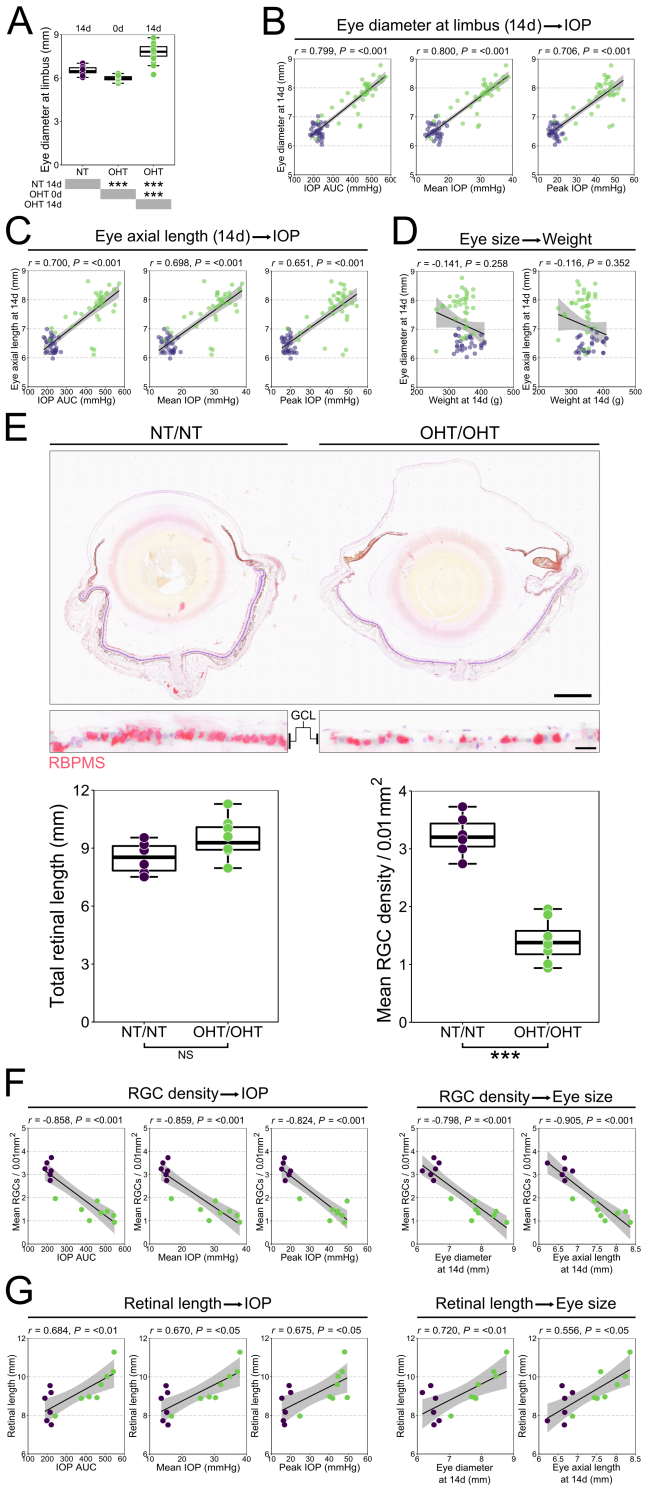
A
14d
0d
14d
Eye diameter at limbus (mm)
NT
OHT
OHT
NT 14d
OHT 0d
OHT 14d
***
***
***
B
Eye diameter at limbus (14d)→IOP
r = 0.799, P = <0.001
r = 0.800, P = <0.001
r = 0.706, P = <0.001
Eye diameter at 14d (mm)
IOP AUC (mmHg)
Mean IOP (mmHg)
Peak IOP (mmHg)
C
Eye axial length (14d)→IOP
r = 0.700, P = <0.001
r = 0.698, P = <0.001
r = 0.651, P = <0.001
Eye axial length at 14d (mm)
IOP AUC (mmHg)
Mean IOP (mmHg)
Peak IOP (mmHg)
D
Eye size→Weight
r = -0.141, P = 0.258
r = -0.116, P = 0.352
Eye diameter at 14d (mm)
Eye axial length at 14d (mm)
Weight at 14d (g)
Weight at 14d (g)
E
NT/NT
OHT/OHT
GCL
RBPMS
Total retinal length (mm)
NT/NT
OHT/OHT
NS
Mean RGC density / 0.01 mm2
NT/NT
OHT/OHT
***
F
RGC density→IOP
r = -0.858, P = <0.001
r = -0.859, P = <0.001
r = -0.824, P = <0.001
Mean RGCs / 0.01mm2
IOP AUC
Mean IOP (mmHg)
Peak IOP (mmHg)
RGC density→Eye size
r = -0.798, P = <0.001
r = -0.905, P = <0.001
Eye diameter at 14d (mm)
Eye axial length at 14d (mm)
G
Retinal length→IOP
r = 0.684, P = <0.01
r = 0.670, P = <0.05
r = 0.675, P = <0.05
Retinal length (mm)
IOP AUC
Mean IOP (mmHg)
Peak IOP (mmHg)
Retinal length→Eye size
r = 0.720, P = <0.01
r = 0.556, P = <0.05
Eye diameter at 14d (mm)
Eye axial length at 14d (mm)

Figure 4: Sustained OHT results in ocular stretch. (**A**) OHT eyes demonstrated a significant increase in diameter by 14 days compared to both pre-surgery size and NT controls. (**B-C**) Eye diameter at the limbus and axial length at day 14 demonstrated reasonable correlation to measures of IOP (AUC, mean, peak), indicating a relationship between the magnitudes of IOP increase and increase in the size of the eye. (**D**) These correlations were not driven by animal age or weight. (**E**) To assess retinal stretch following OHT whole eyes were paraffin embedded and sectioned, and RGCs labelled with antibodies against RBPMS. There was no significant increase in total retinal length following OHT, which was highly variable even across NT eyes. RGC counts across the retina confirmed gross RGC loss. (**F**) RGC density was highly correlated with all measured of IOP and eye size. (**G**) Retinal length correlated with measures of IOP, but to a lesser degree. For complete *n* please see **Methods**. Scale bars = 1 mm in **E** (*upper panel*), 20 µm in **E** (*lower panel*), * = $P < 0.05$, ** = $P < 0.01$, *** $P < 0.001$, NS = non-significant ($P > 0.05$).

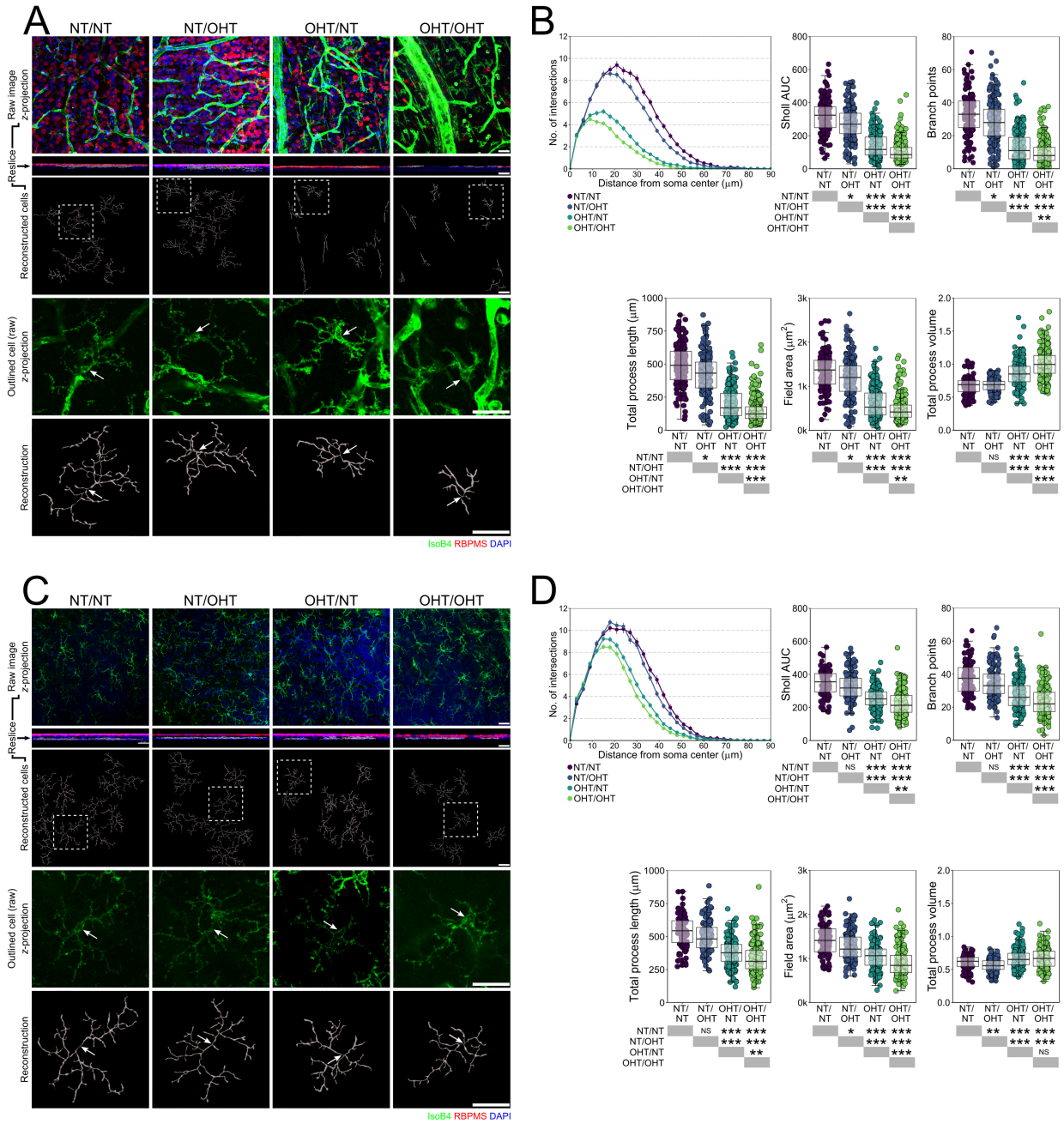
A
NT/NT
NT/OHT
OHT/NT
OHT/OHT
Raw image z-projection
Reslice
Reconstructed cells
Outlined cell (raw) z-projection
Reconstruction
IsoB4 RBPMS DAPI
B
No. of intersections
Distance from soma center (μm)
NT/NT
NT/OHT
OHT/NT
OHT/OHT
Sholl AUC
Branch points
Total process length (μm)
Field area (μm²)
Total process volume
NS
C
D

Figure 5: OHT results in microglia remodelling and activation. (**A**) Morphologies of individual microglia from the NFL/GCL were assessed by high resolution confocal imaging and Imaris reconstructions (*labels to left of image panel*). (**B**) Multiple metrics of microglia morphology demonstrated significant changes in microglia between all groups suggesting progressive activation from NT/NT > NT/OHT > OHT/NT > OHT/OHT (retracted processes of increased volume). (**C-D**) These data were mirrored in microglia from the IPL. For complete *n* please see **Methods**. White arrows denote microglia soma position in **A** and **C**, scale bars = 30 µm in **A** and **C**, * = $P < 0.05$, ** = $P < 0.01$, *** $P < 0.001$, NS = non-significant ($P > 0.05$).

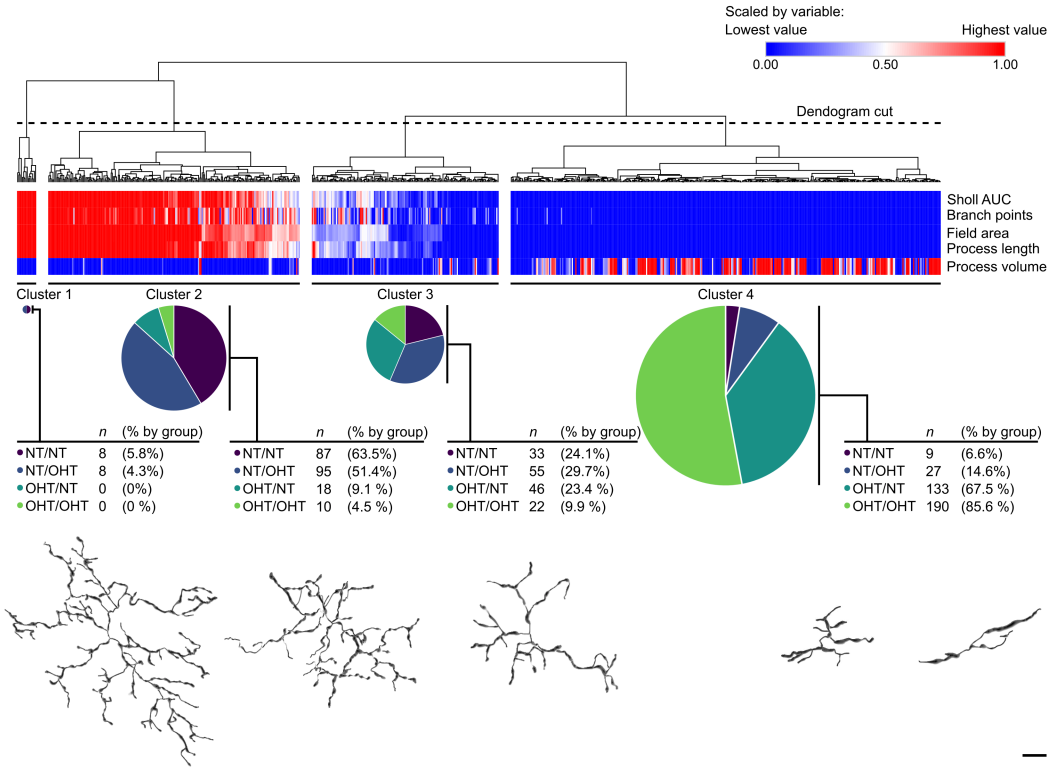

Figure 6: Hierarchical clustering distinguishes activation state and disease groupings. Hierarchical clustering of microglia metrics by Euclidean distance was used to cluster microglia morphologies, generating 4 independent clusters of microglia (Cluster 1-4). The breakdown of each cluster is shown *below* the heatmap/dendrogram. Example cells belonging to each cluster as shown *below* cluster breakdown. Clusters represented groups of activation and demonstrates that microglial morphological measurements can distinguish biologically meaningful groups of microglia independently of disease grouping. *Scale* bar = 10 µm.

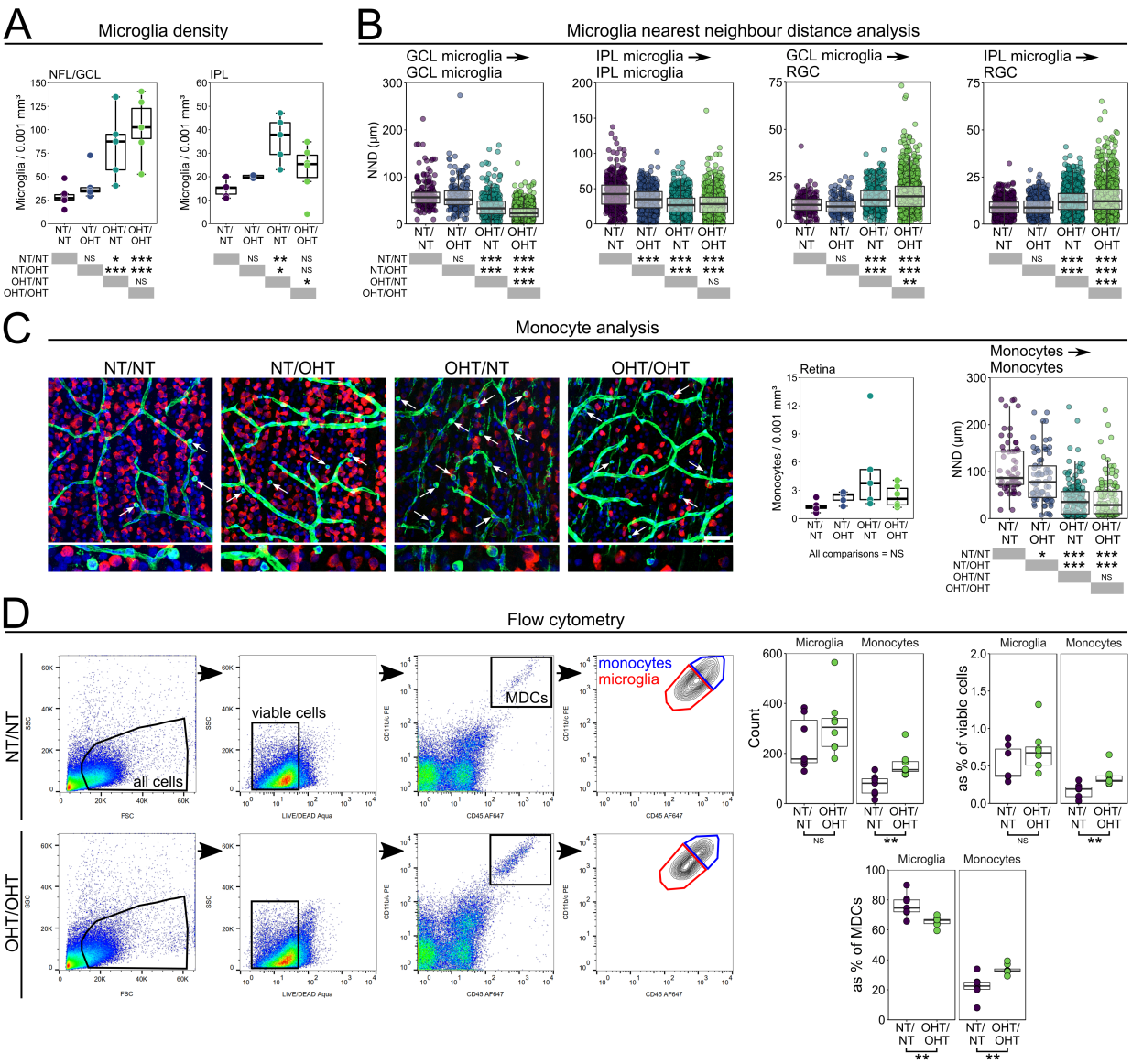

Figure 7: Monocytes enter OHT retina early following IOP elevation. (**A**) Following 14 days of OHT microglia numbers were increased in both the NFL/GCL and IPL of the retina. (**B**) NND analysis demonstrates that microglia get closer to each other but are diffuse around RGCs suggesting that microglia do not cluster around surviving RGCs. (**C**) Ameboid monocytes were present in all conditions after 14 days of OHT (*white arrows*) with small NNDs suggestion monocyte clumping in local regions of damage. (**D**) To begin to assess whether this increase in microglia number was due to infiltrating monocytes entering the tissue and become microglia-like monocyte derived macrophages, whole retina homogenate was assessed by flow cytometry. Retinas were sampled at 3 days post-injection (the point of peak IOP in this model). At this time point microglia numbers were not increased but there was a significant increase in monocyte numbers (both by raw count and as a percentage of other cell types). MDCs = myeloid derived cells. For complete *n* please see **Methods**. Scale bars = 100 µm in **C**, * = $P < 0.05$, ** = $P < 0.01$, *** $P < 0.001$, NS = non-significant ($P > 0.05$).

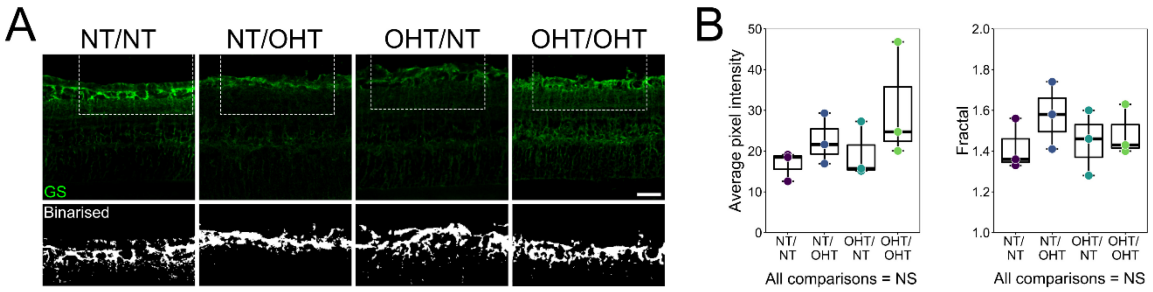

Figure 8: No activation of Müller glia identified by glutamine synthetase labelling. (**A**) Müller glia were labelled in cryo-sections by glutamine synthetase (GS). GS content was assessed in the NFL/GCL/IPL by measuring average pixel intensity and by fractal analysis of binarized crops. (**B**) No significant difference in average pixel intensity or fractal was observed across groups, suggesting no gross Müller glia activation at this time point in this model. Scale bars = 50 µm in **A**, NS = non-significant ($P > 0.05$).

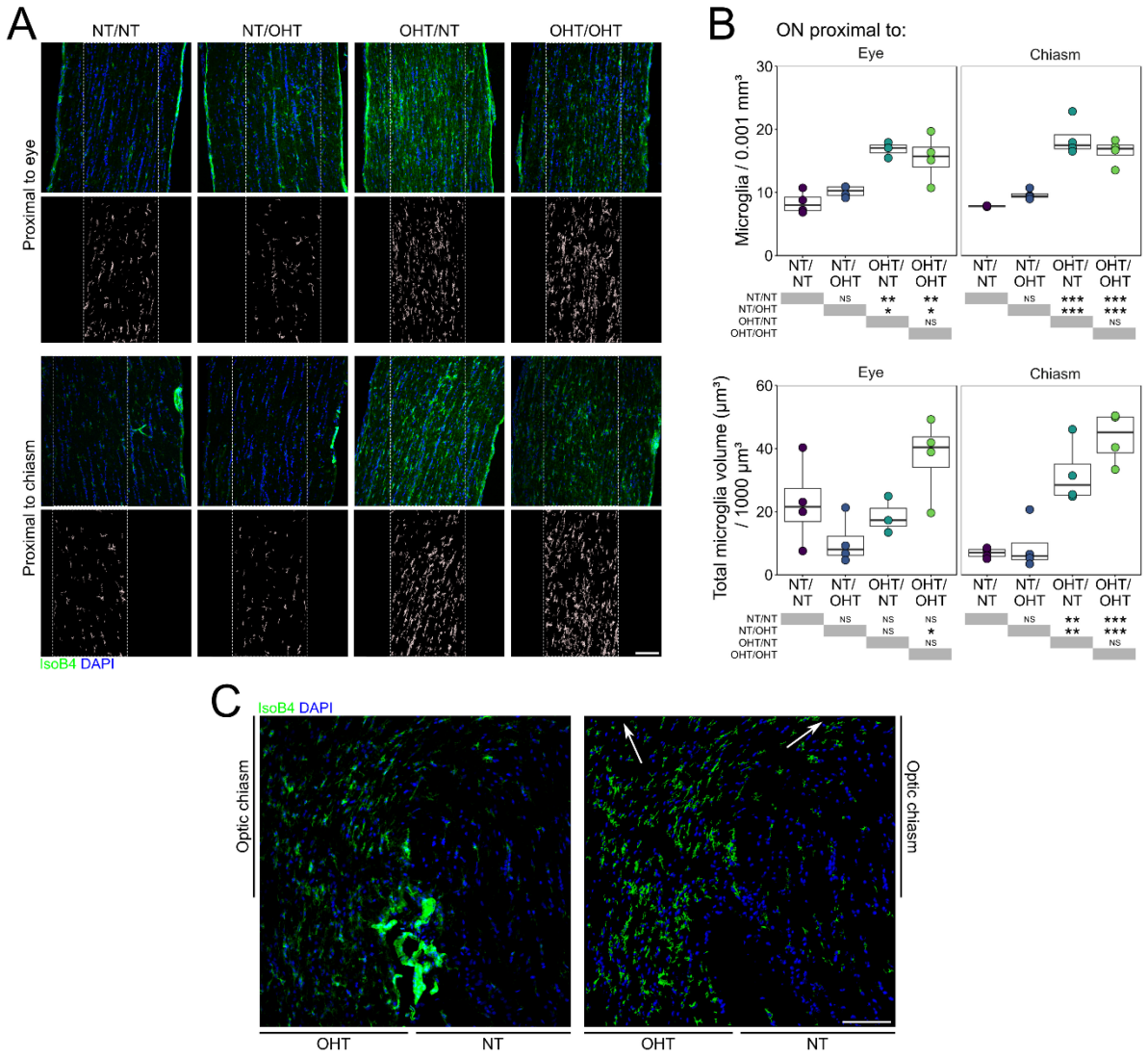

Figure 9: Microglia activation extends into the optic nerve and optic chiasm. (**A**) Optic nerves were transversally sectioned and overall microglial labelling was reconstructed (*insets*) and analysed. (**B**) There exists significant microglia activation in the optic nerve proximal to the eye and proximal to the chiasm. (**C**) Microglial activation is most evidently demonstrated at the chiasm where RGC axons from unilateral OHT animals decussate, with the appearance of activated microglia following both optic tracts post-chiasm (*white arrows* in reconstruction; *right*). Scale bars = 100 µm in **A** and **C**, * = $P < 0.05$, ** = $P < 0.01$, *** $P < 0.001$, NS = non-significant ($P > 0.05$).

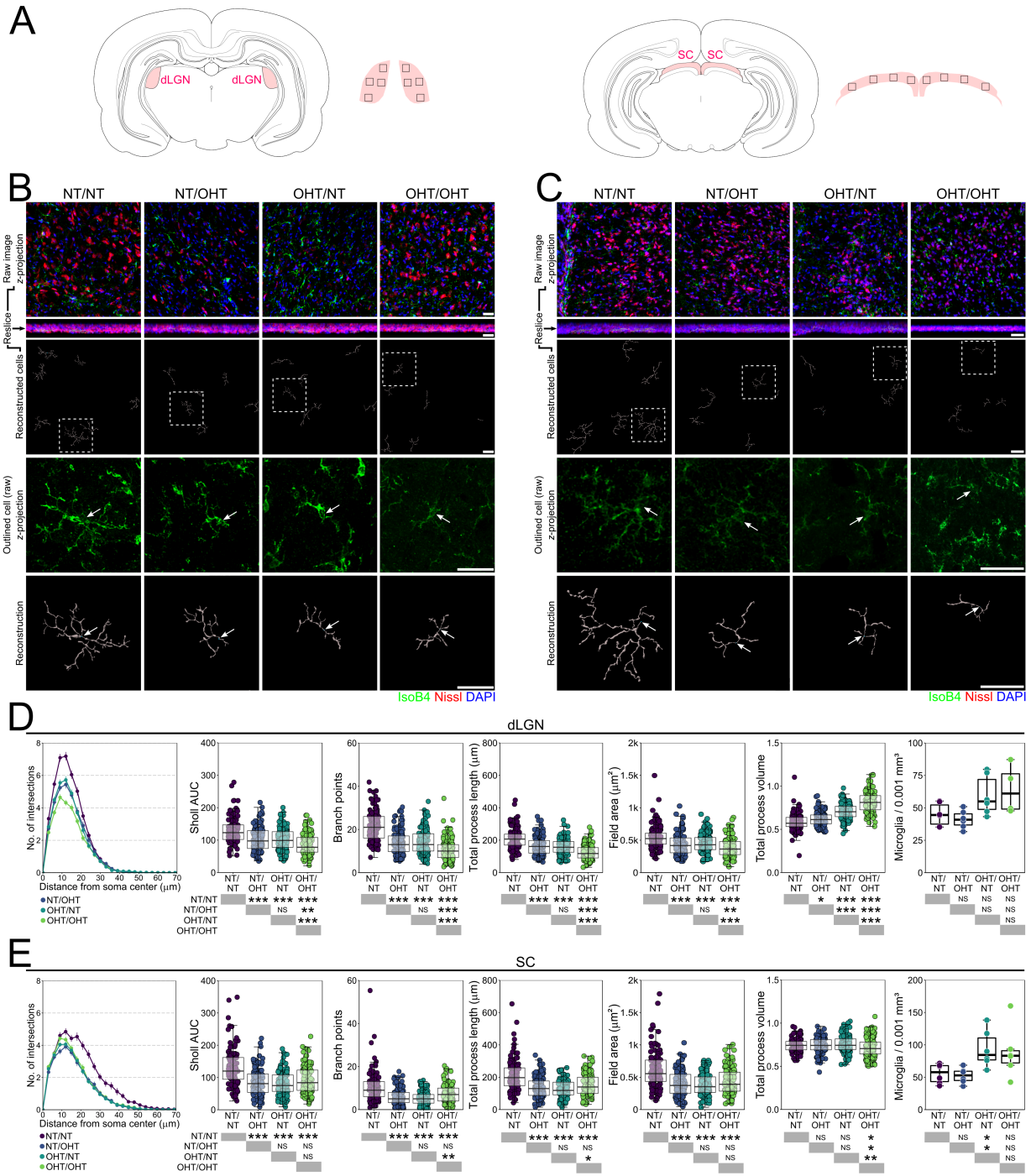
A
dLGN
dLGN
SC
SC
B
NT/NT
NT/OHT
OHT/NT
OHT/OHT
Raw image z-projection
Reslice
Reconstructed cells
Outlined cell (raw) z-projection
Reconstruction
IsoB4 Nissl DAPI
C
NT/NT
NT/OHT
OHT/NT
OHT/OHT
Raw image z-projection
Reslice
Reconstructed cells
Outlined cell (raw) z-projection
Reconstruction
IsoB4 Nissl DAPI
D
dLGN
No. of intersections
Distance from soma center (µm)
NT/NT
NT/OHT
OHT/NT
OHT/OHT
Sholl AUC
Branch points
Total process length (µm)
Field area (µm²)
Total process volume
Microglia / 0.001 mm³
E
SC
No. of intersections
Distance from soma center (µm)
NT/NT
NT/OHT
OHT/NT
OHT/OHT
Sholl AUC
Branch points
Total process length (µm)
Field area (µm²)
Total process volume
Microglia / 0.001 mm³

Figure 10: Microglia activation persists into terminal visual thalami following OHT. (**A**) Microglia were assessed from dLGN and SC sections. Regions of images are shown by black inset boxes in the schematics. Morphologies of individual microglia from the dLGN (**B**) and SC (**C**) were assessed by high resolution confocal imaging and Imaris reconstructions (*labels to left of image panel*). (**D-E**) Multiple metrics of microglia morphology demonstrated significant changes in microglia morphology between NT/NT and all other groups. These results were more binary (*i.e.* damage to a single retina drives neuroinflammatory insults to both terminating hemispheres) suggesting that neuroinflammatory signatures propagate even when only a small percentage of axons are damaged or dystrophic. For complete *n* please see **Methods**. White arrows denote microglia soma position in **B** and **C,** scale bars = 30 μm in **B** and **C**, * = $P < 0.05$, ** = $P < 0.01$, *** $P < 0.001$, NS = non-significant ($P > 0.05$).

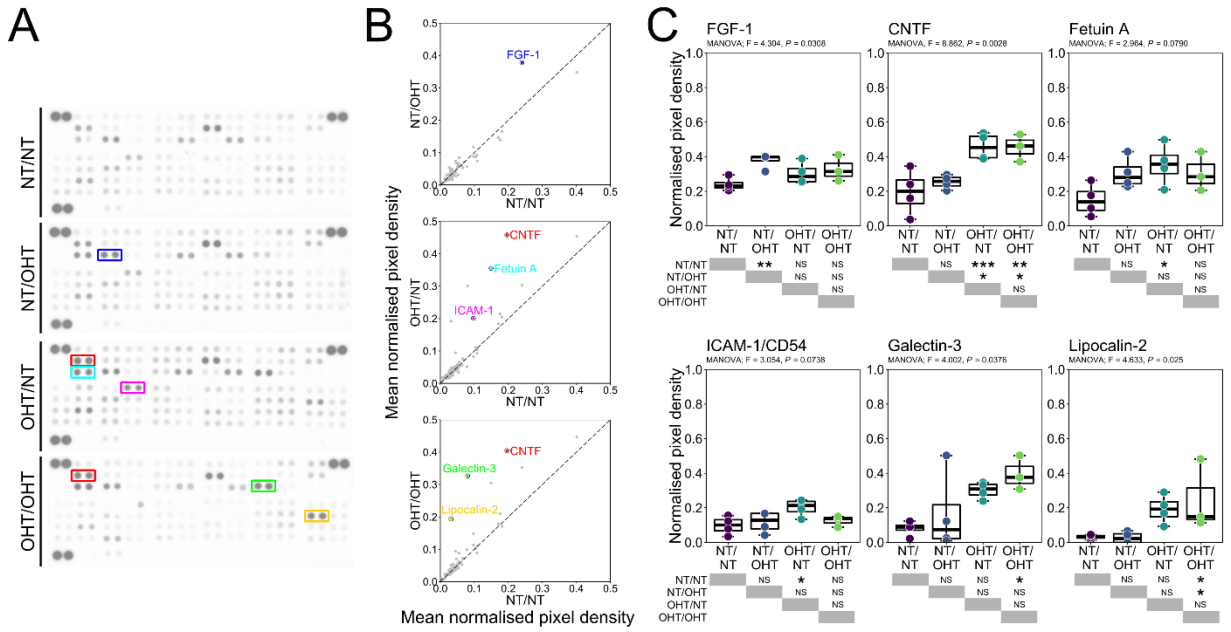

Figure 11: OHT drives neuroinflammatory cytokine expression in the retina. (**A**) To assess cytokine and chemokine expression in the retina following OHT, retinas were homogenized and assessed by protein array. (**B-C**) Densitometry analysis identified 1 changed cytokine (FGF-1) between NT/NT and NT/OHT groups, 3 changed cytokines (CNFT, Fetuin A, ICAM-1) between NT/NT and OHT/NT groups, and 3 changed cytokines (CNTF, Galectin-3, Lipocalin-2) between NT/NT and OHT/OHT groups. All cytokines were increased compared to NT/NT groups and may represent ideal candidates for further experimentation or as biomarker candidates. * = $P < 0.01$, ** = $P < 0.05$, *** $P < 0.01$, NS = non-significant ($P > 0.05$).

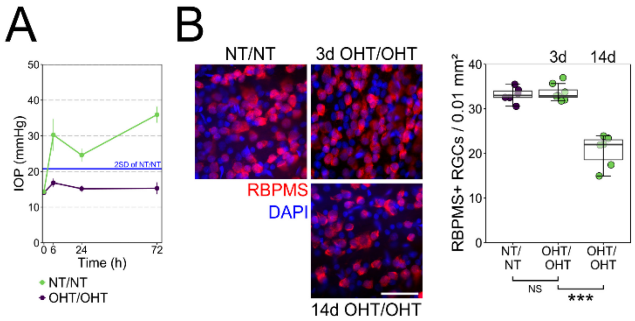

Supplementary Figure 1: IOP peaks at 3 days post-OHT induction with no detectable RGC death. (**A**) IOP measurements were collected 6, 24, and 72 hours post-injection demonstrate that peak IOP occurs at 3 days. (**B**) RGC labelling by RBPMS on flat-mount retinas revealed no significant change in RGC density at 3 days post-OHT induction supporting a pathology absent of early ischemia-related RGC death. For complete *n* please see **Methods**. Scale bars = 50 µm in **B**, *** $P < 0.001$, NS = non-significant ($P > 0.05$).